UNIVERSITY OF OKLAHOMA

GRADUATE COLLEGE

A HIGH CADENCE STUDY OF STELLAR VARIABILITY: SEARCHING FOR HABITABLE PLANETARY COMPANIONS ORBITING WHITE DWARFS WITH THE DECAM MINUTE CADENCE SURVEY

A DISSERTATION

SUBMITTED TO THE GRADUATE FACULTY

in partial fulfillment of the requirements for the

Degree of

DOCTOR OF PHILOSOPHY

By

Kyra C. Dame
Norman, Oklahoma
2019

A HIGH CADENCE STUDY OF STELLAR VARIABILITY: SEARCHING FOR HABITABLE PLANETARY COMPANIONS ORBITING WHITE DWARFS WITH THE DECAM MINUTE CADENCE SURVEY

A DISSERTATION APPROVED FOR THE
HOMER L. DODGE DEPARTMENT OF PHYSICS AND ASTRONOMY

BY

Dr. Mukremin Kilic, Chair

Dr. Nathan Kaib

Dr. John Wisniewski

Dr. Armin Rest

Dr. Trina Hope

Acknowledgements

Like life, science is not done in isolation, and there are many people without whom this dissertation would not exist.

First, to Dr. Mukremin Kilic, thank you for being a wonderful advisor and a constant source of knowledge, suggestions, and support.

Thank you to Evan Rich, Steven Silverberg, Renae Wall, Alek Kosakowski, and the numerous other friends I have made on this crazy journey called grad school. Thank you for friendships forged in the fires of classes and research, for the countless hours of conversations, both physics-related and not, and for cheering me up and cheering me on when needed.

Thank you to my parents for their constant support and enthusiasm, even when they had no idea what I was working on. And thank you to my wonderful Raven, whose constant purring and affection kept me sane these last years, even as she tried her best to drive me crazy (as is a cat's perogative).

Thank you to all of the collaborators who made this work possible: Armin Rest, Alex Gianninas, Sara Barber, and Warren Brown. And a special thank you to Claudia Belardi, without whom I would have no data. Thank you for braving all those days of beautiful Chilean summer and at least one crazy international flight home. I am not jealous, I swear.

Table of Contents

List of Tables

List of Figures

Abstract

One outstanding question in astronomy is what happens to planetary systems as their host star evolves. Though indirect evidence such as metal polluted white dwarf atmospheres and debris disks around white dwarfs, and recent observations of a disintegrating transiting planetesimal around the white dwarf WD 1145+017, suggest that something must survive, we have yet to observe a solid body planetary companion orbiting a white dwarf. In this dissertation, we search the 90219 pount sources identified in the DECam minute cadence survey for evidence of planetary eclipses around white dwarfs, as well as other sources of stellar variability. We find no evidence of eclipse-like events consistent with a planet orbiting a white dwarf, though we do find evidence of two unexpected ∼minute duration dips around the likely M-dwarf J0856−0416. Galaxy models predict 802 white dwarfs in the survey, and we constrain the occurrence rate for habitable earth-sized planets around white dwarfs to $\leq 37\%$ at the 95% confidence level, consistent with previous studies when adjusted for differences in sample size. Additionally, we detect 132 variable systems, 97 of which are new detections. We find 77 binary systems, including two eclipsing white dwarf + M dwarf systems and one system containing a likely extremely low mass white dwarf, 29 δ Scuti pulsators, 13 RR Lyrae, seven ZZ Ceti pulsators, two of which appear massive enough to have begun crystallization, and six sources of unidentified variable type.

Chapter 1

Introduction

1.1 White Dwarfs

White dwarfs are the final stage of evolution for stars with initial masses $\leq$ 8-10 $M_{\odot}$(Iben et al., 1997). As these low mass stars evolve, mass loss and stellar winds strip the outer layers of the star, leaving behind a degenerate core composed of carbon and oxygen surrounded by a thin atmosphere of hydrogen and/or helium. These stellar remnants have typical masses around 0.6 $M_{\odot}$, but radii comparable to Earth ($\approx$ 0.01 $R_{\odot}$), and are supported by electron degeneracy pressure. By this point, nuclear processes in the core have long since ceased, and white dwarfs spend the remainder of their lives radiating energy as they cool. This makes them relatively easy to understand and model. Model fits of spectroscopic or photometric data yield effective temperatures and surface gravities, which can then be used to calculate masses, radii, luminosities, and cooling ages (Bergeron et al., 2001). It is worth noting that photometric data must usually be combined with parallax measurements in order to break degeneracies in the models.

Due to their inherent faintness, white dwarf research has historically suffered from small sample sizes compared to other fields. White dwarfs can be identified through UV excesses or reduced proper motion. Reduced proper motion is defined as $H = m + 5\log\mu = M + 5\log V_{tan} - 3.379$, where m is the apparent magnitude of the white dwarf, μ is the proper motion, M is the absolute magnitude, and V_{tan} is the tangential velocity in km s^{-1}. For samples with similar kinematics, reduced proper motion can serve as a proxy for absolute magnitude, yielding relatively clean samples for white dwarfs with $\mu > 20$ mas yr^{-1} (See Figure 1.4). The Sloan

Digital Sky Survey (SDSS) and other large-area spectroscopic surveys drastically increased the number of spectroscopically confirmed white dwarfs to $\approx$ 33,000 (Kleinman et al., 2013; Kepler et al., 2016). However, this sample was biased towards inherently brighter hot, young white dwarfs. With the release of Gaia Data Release 2, the number of white dwarf candidates has exploded, with Gentile Fusillo et al. (2019) identifying $\approx$ 260,000 high-confidence white dwarf candidates down to *Gaia* magnitudes G < 21.

Though they represent the end of a star's life, white dwarfs are an important tool in modern astronomy. Because ages can be computed from cooling models, white dwarfs provide independent ages estimates of Galactic populations such as the disk and halo. Galactic ages can be estimated through either individual field white dwarfs (Kalirai, 2012; Dame et al., 2016; Kilic et al., 2019), with the assumption that a given Galactic population must be at least as old as the oldest star in it, or through the White Dwarf Luminosity Function (WDLF, Holberg et al., 2016; Munn et al., 2017; Kilic et al., 2017), which uses the peak in the distribution of white dwarf magnitudes for a Galactic population to estimate the population's age. As a note, one of the biggest challenges with getting ages from the WDLF has always been a lack of faint white dwarfs, especially for the Galactic halo. Additionally, asteroseismology can probe the interior of pulsating white dwarfs, providing information about dense plasma physics and core crystallization (Giammichele et al., 2017). White dwarfs are also thought to be the progenitors of Type Ia supernovae, which were used to confirm the accelerated expansion of the universe. Short period binary white dwarf systems will serve as useful calibration sources for the upcoming *LISA* mission, providing constraints on the expected gravitational wave foreground (Korol et al., 2019). In this dissertation, we consider white dwarfs as potential hosts for planetary systems.

1.2 Planetary Companions to Main Sequence Stars

There are currently thousands of known exoplanets, with over 90% found around low mass main sequence stars that will one day become white dwarfs (Veras, 2016). Petigura et al. (2013) found that $\approx$ 22% of main sequence stars host habitable earth-sized planets. The most common methods for detecting exoplanets are the transit method, which looks for the decrease in a star's light as a planet passes in front of it, and the radial velocity method, which looks for Doppler shifts in the star's spectrum due to the gravitational influence of a planet. Figure 1.1 shows the masses and radii as a function orbital separations for currently known exoplanets. Earth-sized planets being far more common than Jupiter-sized planets. Red points are planets detected via the transit method, and blue points are planets detected via radial velocity methods. The majority of planets discovered via the transit method have small orbital separations because these systems have higher transit probabilities and more transits can be observed for a given baseline. In contrast, the radial velocity method can detect planets over a wider range of orbital separation, but has trouble detecting lower mass planets.

One of the biggest hurdles to finding exoplanets is the host star itself. Figure 1.2 shows the mass and radius of known exoplanets as a function of host star mass. Though planet formation models such as Kennedy & Kenyon (2008) and Alibert et al. (2011) suggest that the fraction of stars hosting giant planets should increase up to 3 $M_{\odot}$, the majority of known exoplanets are found around $\approx$ 1 $M_{\odot}$stars, with only a handful detected around stars with masses $\geq$ 3 $M_{\odot}$. This inconsistency is a reflection of the weaknesses in current planet detection techniques. More massive stars are less likely to be affected by the gravitational influence of planets, and the dimming caused by transiting planets is more likely to get lost in their higher luminosities.

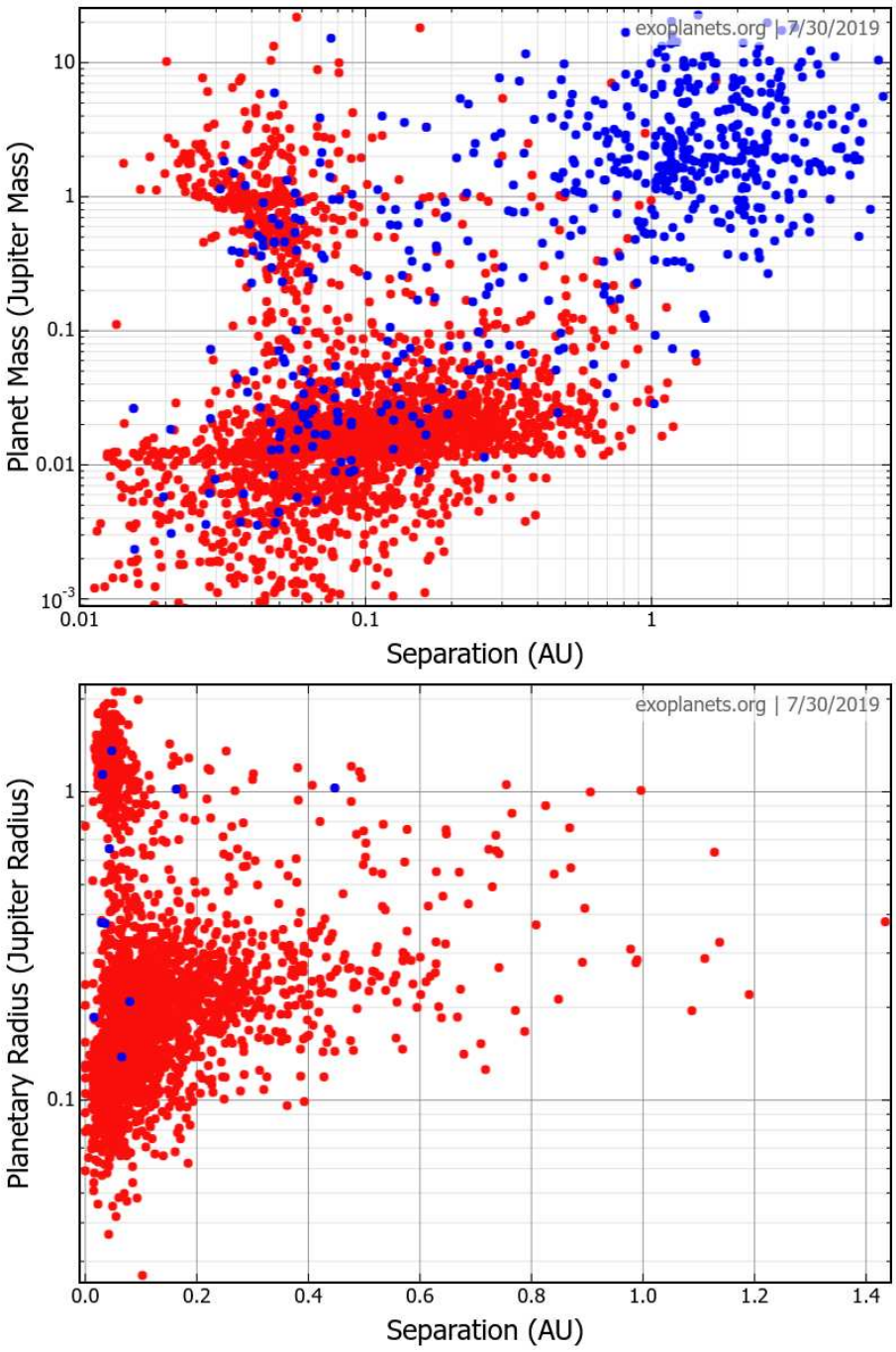

Fig. 1.1.— A graph of planetary mass (top) and radius (bottom) as a function of orbital separation for all currently known exoplanets. Red points are planets detected via transits, and blue points are planets detected via radial velocity.

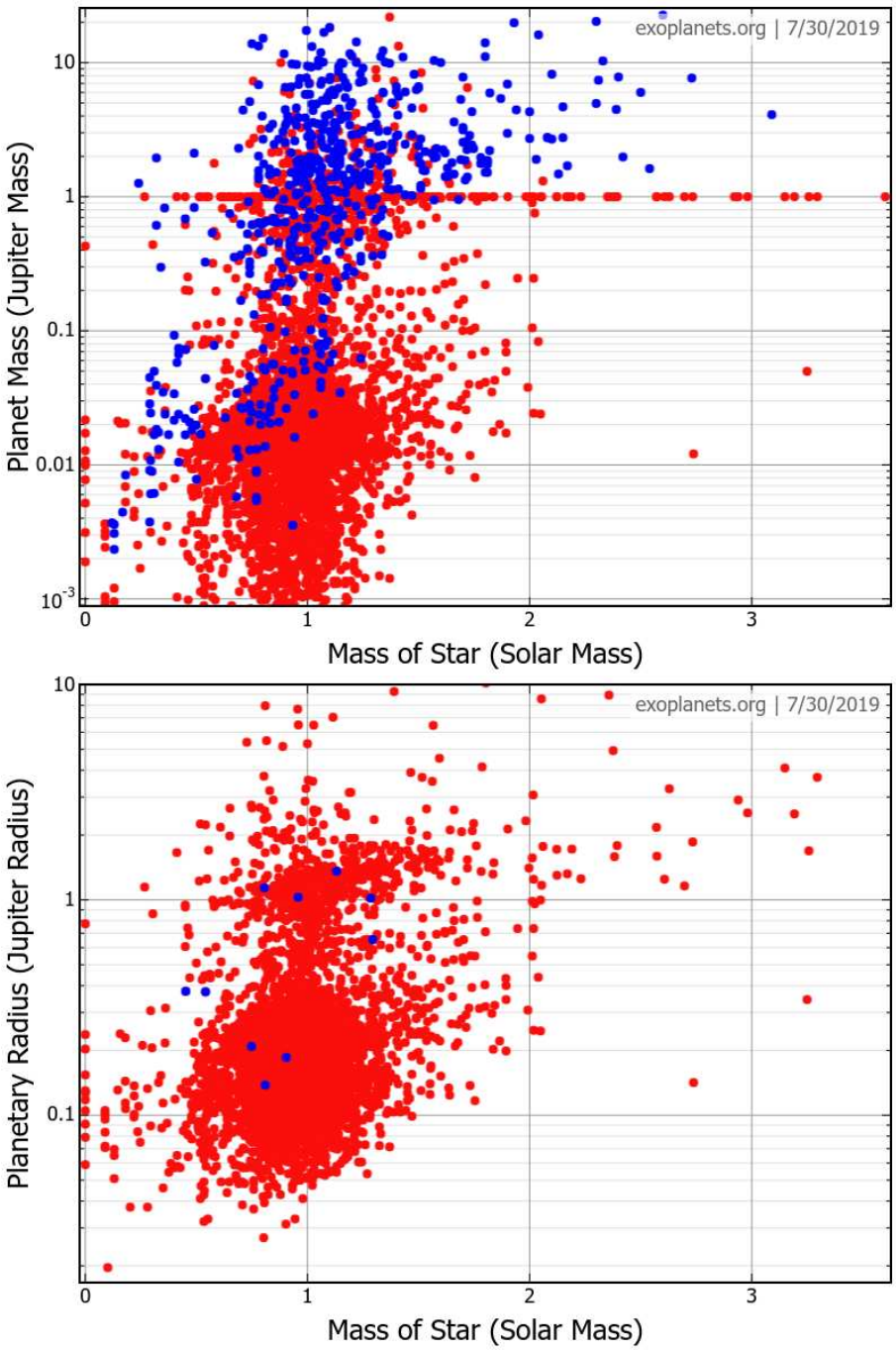

Fig. 1.2.— A graph of planetary mass (top) and radius (bottom) as a function of the mass of the host star for all currently known exoplanets. Colours are the same as Figure 1.1.

White dwarfs offer an alternative way to probe the frequency of planets around main sequence stars by searching for remnant planetary systems in the form of debris discs. This method offers many advantages over traditional planet detection methods. Debris discs cover a much larger area than planets, making them brighter and easier to detect. The signal strength of the disc does not depend on the mass of the white dwarf, allowing us to probe the frequency of planets around a wider range of main sequence progenitor masses. Finally, debris discs can offer insights into regimes that are difficult or impossible to probe with traditional planet detection methods, such as face-on systems or systems with wide orbital separations. Barber et al. (2016) calculated the frequency of debris discs around white dwarfs as a function of mass. They found the frequecy peaked for systems with main sequence progenitor masses around 3 $M_{\odot}$before falling off at higher masses, in agreement with predictions from Kennedy & Kenyon (2008).

1.3 Planetary Companions to White Dwarfs

To date, there have been no definitive detections of any solid body planetary companion orbiting a white dwarf. From a theoretical perspective, such results are unsurprising. Veras (2016) provides a detailed analysis of the effects of post-main sequence evolution on planetary systems. Briefly, the evolution of planetary systems is affected by two competing forces. As the host star evolves through the giant branch, it will expand to engulf close-in planets, resulting in tidal disruption for all but the most massive planets. However, mass loss during this phase will weaken the gravitational pull of the star and cause orbits to expand, potentially saving some planets on the edge of engulfment.

Villaver & Livio (2007) studied the theoretical survival of gas giants around stars with main squences masses in the range 1-5 $M_{\odot}$. They found planets with

initial orbits within the maximum stellar radius of their host star during the giant phase will be engulfed and destroyed for planetary masses less than 15 M_{jup} for a 1 $M_{\odot}$star and less than 120 M_{jup} for a 5 $M_{\odot}$star. They also found that for planets around stars with M $\geq$ 2.5 $M_{\odot}$, the expected orbital separation is $\geq$ 15 AU due to the effects of mass loss on the planet's orbit. However, Veras et al. (2019) found that high-viscosity planets are more likely to survive than low-viscosity ones, and low-mass planets are more likely to survive than massive Super-Earths.

Additionally, observations of white dwarfs provide indirect evidence that something must survive the post-main sequence evolution of the host star. Debris discs are observed around about $1.5^{+1.5}_{-0.5}$ per cent of white dwarfs (Wilson et al., 2019) and 25-50% show pollution from metals in their atmosphere that should have long since sank to the core (Koester et al., 2014). Work by Veras et al. (2014) showed that accretion of comets from exo-Oort clouds was not sufficient to account for the observed metal pollution. In the case of both the debris discs and metal pollution, the composition is consistent with tidally disrupted rocky bodies.

Agol (2011) proposed expanding current searches to find habitable Earth-sized planets to include cool white dwarfs ($T_{eff} \leq 10^4$ K), which are photometrically stable enough to allow detection of such planets. Because white dwarfs cool as they age, the location of their habitable zone, where a planet could maintain liquid water on its surface, will change over time. Agol (2011) defines the continuous habitable zone (CHZ) for white dwarfs as the region such that a planet within that region would remain habitable for at least 3 Gyr. From this definition, the CHZ extends from $\approx$ 0.005 to 0.02 AU for white dwarfs with temperatures less that 10^4 K and masses between 0.4 and 0.9 $M_{\odot}$, corresponding to orbital periods of $\approx$ 4-32 hours. The lower bound corresponds to the Roche limit for the white dwarf, interior to which a planet would be tidally disrupted. Planets beyond 0.02 AU would not remain habitable for the required 3 Gyr duration. Figure 1.3 shows the

CHZ as a function of the orbital distance of the planet and white dwarf mass for a hydrogen atmosphere white dwarf, as well as how the outer boundary changes for different habitability timescales.

Solid body transits of white dwarfs occur on minute timescales. Previous large area transient surveys with cadences of hours to days, such as the the Sloan Digital Sky Survey Stripe 82 (Bramich et al., 2008), the Panoramic Survey Telescope Rapid Response System (Pan-STARRS) Medium Deep fields (Tonry et al., 2012), and the Catalina survey (Drake et al., 2013, 2014), are ill-suited to detect such brief events. Exoplanet surveys such as the Wide Angle Search for Planets (WASP, Pollacco et al., 2006) and the Hungarian-made Automated Telescope Network (HATNet, Bakos et al., 2004) have the cadence required to detect these short duration eclipses but are limited to bright stars, providing 1 per cent photometry only for stars brighter than 12 mag. The *Kepler/K2* mission imaged more than 1000 white dwarfs, resulting in the first detection of a disintegrating planetesimal orbiting the white dwarf WD 1145+017 (Vanderburg et al., 2015; Gänsicke et al., 2016; Rappaport et al., 2016). Recently, Manser et al. (2019) found evidence in short cadence spectroscopy of variation in the Ca II triplet caused by a solid-body planetesimal orbiting the white dwarf SDSS J1228+1040, speculated to be the leftover core of a planet. Previous studies have also used Pan-STARRS (Fulton et al., 2014), *Kepler/K2* (Van Sluijs & Van Eylen, 2018), and *GALEX* (Rowan et al., 2019) data to constrain the occurrence rate of planets around white dwarfs. Van Sluijs & Van Eylen (2018) constrained the occurrence rate for planets with radii $\leq 2\ R_{\oplus}$ to <28%.

The DECam minute cadence survey was the first high cadence survey of its kind, designed specifically to search for planetary companions to white dwarfs. It makes use of the Dark Energy Camera (DECam), made of 62 individual CCDs, mounted on the 4-m Blanco telescope. However, two CCDs were not functioning

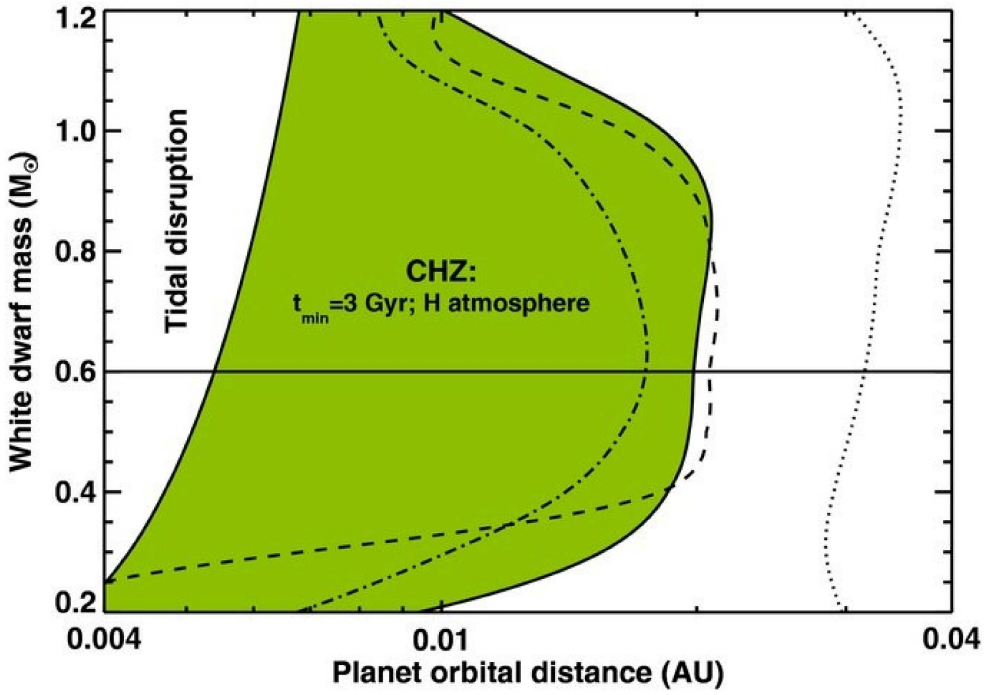

Fig. 1.3.— CHZ vs. white dwarf mass and planet orbital distance. Green region is the CHZ for $t_{HZ} > t_{min} = 3$ Gyr, H atmosphere. Left solid line is Roche limit for Earth-density planets. The other lines show how the CHZ outer boundary changes for $t_{min} = 1$ Gyr (dotted line), for $t_{min} = 5$ Gyr (dash-dotted line), or for an He atmosphere with $t_{min} = 3$ Gyr (dashed line). Horizontal lines indicates the most common white dwarf mass of $0.6 M_{\odot}$. Figure from Agol (2011).

during our observations, reducing the number of useable CCDs to 60. Each CCD is 2048 x 4096 pixels and has a platescale of 0.263" per pixel. The 3 deg^2 field of view of DECam allows for continuous imaging of hundreds of white dwarfs every night. We obtained g-band images spanning eight half-nights for three separate DECam pointings (hereafter referred to as fields), or 9 deg^2 of the sky, with ≈ 90 second cadence. Exposure times were chosen to yield S/N ≥ 5 for sources brighter than $g = 24.5$ AB mag. Fields were chosen to be visible from the 4-m Blanco telescope and overlap with the Canada-France-Hawaii Telescope Legacy Survey (CFHTLS, Cuillandre et al., 2012) Wide 2 field. This choice provides Megacam *ugriz* photometry and colours for our entire survey, and high cadence imaging for approximately one third of the CFHTLS Wide 2 Field. Initial work focused on 111 high proper motion white dwarfs identified in the first field. Figure 1.4 shows the reduced proper motion diagram for the first DECam field, with white dwarf candidates shown as green and yellow points. Belardi et al. (2016) found no evidence of planetary eclipses around these white dwarfs, but they note that galaxy models predict hundreds of white dwarfs in the field with proper motions too low to be identified by cuts in reduced proper motion.

1.4 Stellar Variability

There are two categories of stellar variability. Intrinsic variability, such as pulsations and flares, are due to changes in the physical properties of the star itself, while extrinsic variability is caused by some external factor, such as a companion or rotational effects. All of the systems in this dissertation with determined variable type are either binary systems or pulsators, so these are the types of variability on which we focus. Example light curves for each type of variability can be found in Section 2.4. Because periodic variability is the easiest to detect, we

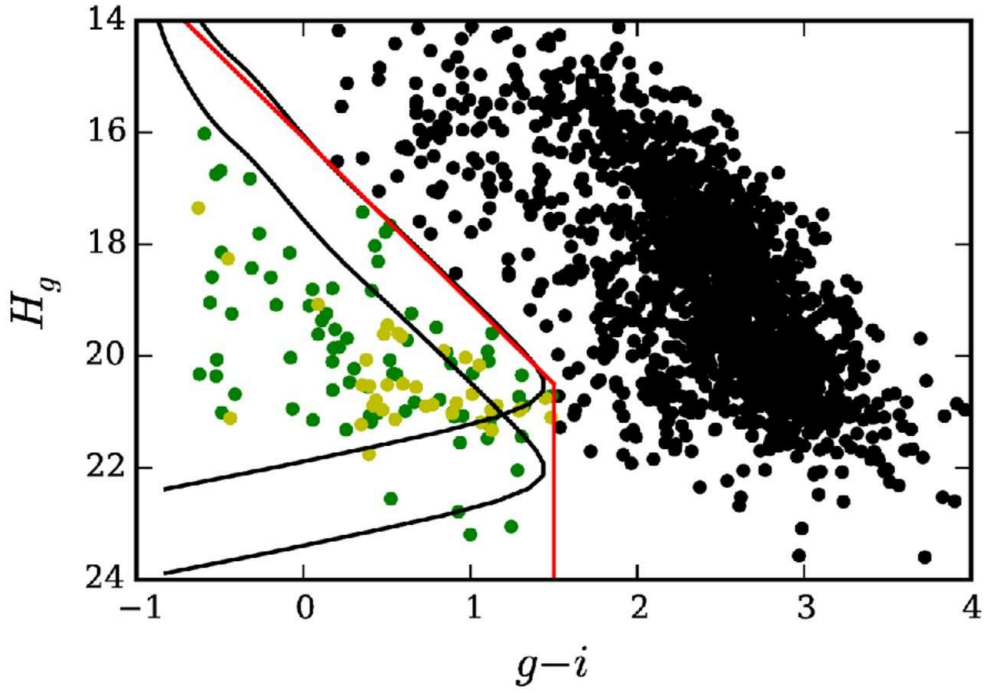

Fig. 1.4.— The reduced proper motion diagram for stars in the first DECam field. White dwarf cooling curves for tangential velocities of 20 and 40 km $s^{-1}$are shown as solid lines. the red line delineates the area of interest for white dwarfs. Each object in this region is visually inspected and classified as 'good' (green) and 'maybe' (yellow) white dwarf candidates. Figure from Belardi et al. (2016).

only consider periodically variable objects, which we will consistently refer to as simply "variable objects" throughout this work. Based on the longest determined period in our sample, we are sensitive to variability with periods up to at least 4 days.

Binary systems can be further separated as contact binaries and detached binaries. Contact binaries are binary systems where the stars orbit close enough to touch, allowing mass transfer as the stars overfill their Roche lobes. While such systems may show traditional eclipses depending on the inclination angle of the system, the variability exhibited in their light curves is most often a result of ellipsoidal variation, as the gravity of each star deforms its companion and changes the visible area as the stars orbit. Their light curves show continuous variability with periods of less than a day. Detached binaries are systems with orbits large enough that there is little or no mass transfer between stars. Additionally, main squence detached binaries show little to no ellipsoidal variation (ellipsoidal variations can be seen in detached WD binaries due to their significantly higher surface gravities), and the variability in these systems can only be detected through eclipses, as one star passes in front of the other. Their light curves show distinct transits separated by periods of quiescence. These systems can have orbital periods ranging from hours to years.

There are many classes of pulsating stars. Figure 1.5 shows the locations of these classes on the Hertzsprung-Russell diagram. Here we focus on short period ($\leq$ a few days) pulsating stars located in the instability strip, i.e. RR Lyrae, δ Scuti, and ZZ Ceti (also known as DAV) white dwarfs. For stars in the instability strip, pulsations are due to the κ-mechanism, which requires a layer of partially ionized material below the stellar surface. The opacity function has the form κ α $\rho T^{-3.5}$ (where ρ is the density of the region and T is the temperature), so as the temperature of the star increases, opacity typically decreases. However, in

regions of partial ionization, the energy released by contraction can be used to further ionize the region instead of increasing its temperature. Therefore, as the star contracts, the density of the region increases while the temperature remains relatively constant, leading to an increase in opacity in the region. If this partially ionized layer is in a region where radiation is the dominant form of energy transport, this increased opacity will trap energy in the layer and cause the interior of the star to heat up. As the inner temperature rises, the star will begin to expand, causing the partially ionized layer to cool and recombine. This will lead to a decrease in the opacity of the layer, releasing the previously trapped energy as the star once again begins to contract and the cycle begins again. Figure 1.6 shows a diagram of this pulsation cycle.

The differences between different classes of pulsators in the instability strip are largely a matter of stellar luminosity class. δ Scuti are main sequence stars born on the instability strip, RR Lyrae are giant and horizontal branch stars, and ZZ Ceti are white dwarf stars. In the latter two cases, the star is merely evolving through the instability strip, and will only remain variable for a fixed period of time. As the pulsation period is dependent on the size of the star, each type also has its own range of periods, from a few hours to about a day for RR Lyrae to a few hours for δ Scuti to $\leq$ 25 minutes for ZZ Ceti. Another notable difference is that RR Lyrae and δ Scuti pulsate due to partial ionization of He II, while ZZ Ceti, as white dwarfs with hydrogen atmospheres, pulsate due to partial ionization of HI. However, the underlying cause of these pulsations is the same.

1.5 Dissertation Summary

In this dissertation, we search for eclipse events consistent with a planetary companion orbiting a white dwarf around the 90219 point sources detected in the

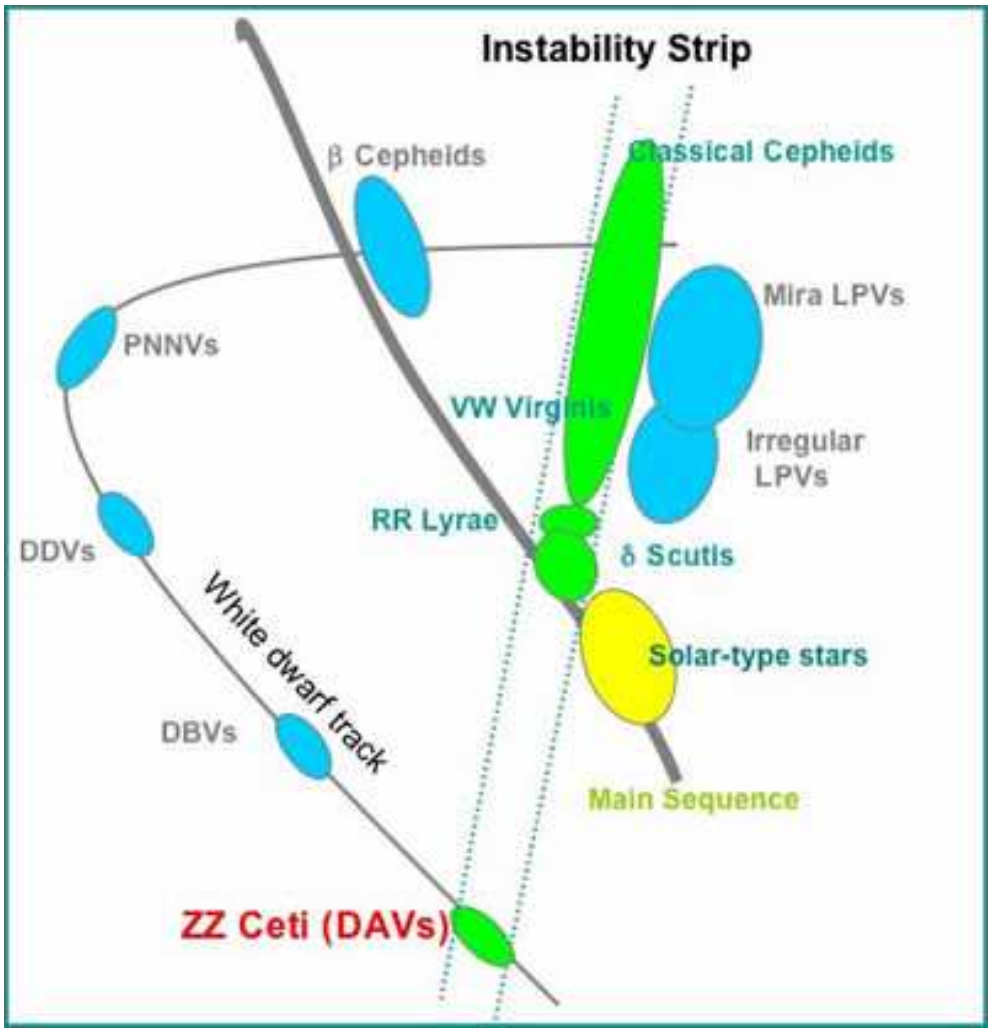

Fig. 1.5.— The Hertzsprung-Russell diagram showing the main sequence (thick gray line) and white dwarf track (thin gray line). The instability strip is denoted by dashed lines. Classes of pulsating stars within the instability strip are shown in green, while other classes of pulsators are shown in blue. Solar type stars are shown in yellow. Figure from http://astronomy.swin.edu.au (Swinburne University of Technology).

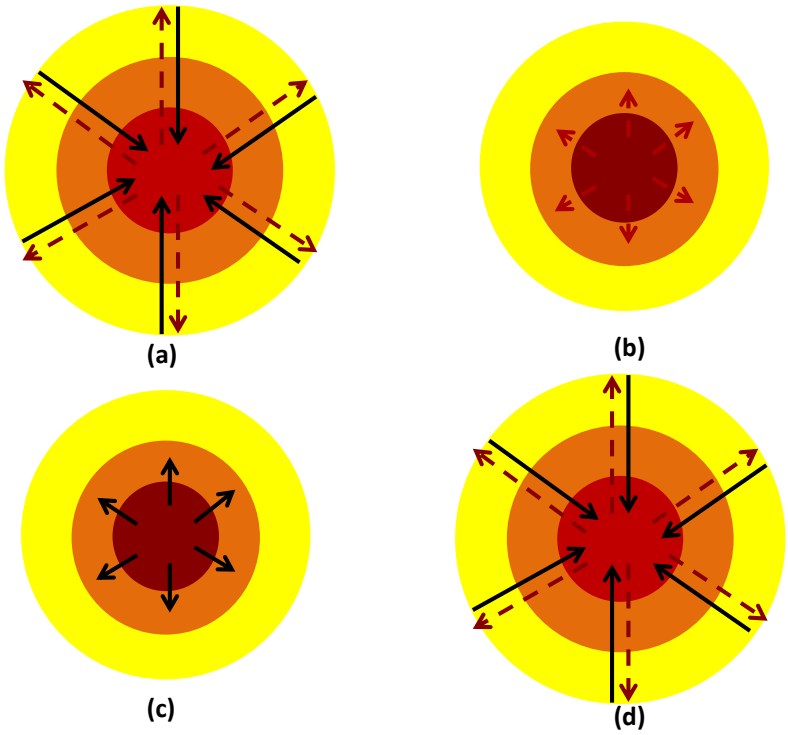

Fig. 1.6.— A diagram of a typical pulsation cycle. (a) The star contracts (black arrows), and energy is released (red arrows). (b) As the opacity in the partial ionization layer (orange) increases, energy becomes trapped in this layer, causing the core temperature to increase. (c) The increased temperature in the core causes the star to expand, cooling the star. (d) The star once again begins to contract and release energy.

DECam minute cadence survey, ensuring that our search does not miss any low proper motion white dwarfs. We then use the photometry from the CFHTLS to determine if the source has colours consistent with a white dwarf. Based on the Besançon Galaxy model (Robin et al., 2003), we expect the survey to contain $\approx$ 1000 white dwarfs. We use our results to constrain the occurrence rate of habitable Earth-like planets around white dwarfs. Additionally, we search for other sources of stellar variability and assemble a catalog of variable stars in our fields. In Chapter 2, we present the results of Dame et al. (2019), in which we present our results from the first DECam field. Chapter 3 is in preparation for submission to MNRAS, and discusses results from the remaining two fields, including constraints on the occurrence rate of habitable earth-like planets around white dwarfs. Finally, we summarize our results and discuss future possibilities in Chapter 4.

This dissertation does not include a discussion of our work on ultracool and halo white dwarfs, which found the coolest currently known pure H atmosphere white dwarf and 5 new halo candidates. Additional information on this work can be found in Dame et al. (2016).

Chapter 2

The DECam Minute Cadence Survey II: 49 Variables but No Planetary Transits of a White Dwarf

2.1 Introduction

Stellar variability on short timescales has been largely unexplored until recently, but is relevant in the era of transient surveys like the Zwicky Transient Facility (ZFT, Bellm & Kulkarni, 2017), the Large Synoptic Survey Telescope (LSST, Ivezic et al., 2008), and in searches for optical counterparts to gravitational wave events detected by the Laser Interferometer Gravitational-Wave Observatory (*LIGO*). Exoplanet surveys like the Wide Angle Search for Planets (WASP, Pollacco et al., 2006) and the Hungarian-made Automated Telescope Network (HATNet, Bakos et al., 2004) have provided ~ 10 minute cadence observations of relatively bright stars, which can be used to search for transits around compact objects like white dwarfs (Faedi et al., 2011). On the fainter end, the Sloan Digital Sky Survey Stripe 82 (Bramich et al., 2008), the Panoramic Survey Telescope & Rapid Response System (Pan-STARRS) Medium Deep Fields (Tonry et al., 2012), and the Palomar Transient Factory (PTF, Rau et al. 2009) provided nightly observations of large areas of sky that were specifically designed to detect supernovae. Fulton et al. (2014) used the Pan-STARRS data on ~ 1700 photometrically selected candidates to constrain the frequency of gas giant planets orbiting white dwarfs just outside the Roche limit (0.01 AU) to $< 0.5\%$, but their cadence and sensitivity were not high enough to constrain the frequency of Earth-size planets

at the same orbital separation.

The Kepler/K2 mission has provided short-cadence, 1 min, data for hundreds of objects, but mainly for previously known pulsating stars. K2 long-cadence data led to the discovery of a disintegrating asteroid around the dusty white dwarf WD 1145+017 (Vanderburg et al., 2015; Gänsicke et al., 2016; Rappaport et al., 2016). Such planetesimals had never been found around white dwarfs previously due to a lack of extended duration high-cadence observations of a large number of white dwarfs. Van Sluijs & Van Eylen (2018) used long and short cadence K2 data from 1148 confirmed and high-probability white dwarfs to constrain the frequency of Earth-sized planets in the habitable zone around white dwarfs to $< 28\%$. For white dwarfs with masses between 0.4 and 0.9 $M_{\odot}$and $T_{\rm eff} < 10000$ K, the continuously habitable zone (the region where a planet could sustain liquid water for > 3 Gyrs) extends from ≈ 0.005 to 0.02 AU (Agol, 2011).

The OmegaWhite Survey (Macfarlane et al., 2015, 2017; Toma et al., 2016) is observing 400 deg^2 of the sky along the Galactic Plane with a median cadence of 2.7 min, with the goal of finding short period ($P_{orb} < 80$ min) variables, especially ultracompact binaries as these are predicted to be the strongest emitters of gravitational waves in the milli-Hertz frequency range (Amaro-Seoane et al., 2013; Roelofs et al., 2007). However, the 2 hour duration of their observations is not ideal for finding transits around white dwarfs as planets with such short periods would be tidally disrupted (Agol, 2011).

The DECam Minute Cadence Survey (Belardi et al., 2016) was the first high cadence survey of its kind, observing 9 deg^2 of the sky at a cadence of ≈ 90 sec over 8 half-nights per field, specifically looking for transits around a large number of white dwarfs. Initial results from this survey focused on 111 high proper motion white dwarfs in their first 3 deg^2 field. While Belardi et al. (2016) did not find evidence of planetary mass companions to these high proper motion white dwarfs,

they note that there should be hundreds of white dwarfs with low proper motion ($\mu < 20$ mas yr^{-1}) in the same field. Here we extract and analyse the photometry for all of the point sources in this field to search for transiting and variable objects, including the lower proper motion objects.

We discuss the details of our observations and reductions in Section 2.2. We discuss the results of our transit search in Section 2.3, present our selection process and list of variable objects in Section 2.4, and conclude in Section 2.5.

2.2 Observations and Data Reduction

2.2.1 DECam Observations

We used the Cerro Tololo Interamerican Observatory 4m telescope equipped with the Dark Energy Camera (DECam) over eight half-nights in Feb 2014. We obtained g-band exposures of a three square degree field, centred at RA = 09:03:02 and Dec = -04:35:00 and previously observed by the Canada-France-Hawaii Telescope Legacy Survey (CFHTLS, Cuillandre et al., 2012) with Megacam *ugriz* photometry available. Our DECam field covers a small portion of the CFHTLS Wide 2 Field. Exposure times were chosen to obtain S/N ≥ 5 photometry of targets brighter than $g = 24.5$ AB mag, giving an overall cadence of ≈ 90 s, including the 20 s read-out time of the camera. Further details of the observations can be found in Belardi et al. (2016).

2.2.2 Photometric Data Reduction

We downloaded the raw DECam data from the NOAO Archive and used the Photpipe pipeline, which was previously used in time-domain surveys like SuperMACHO, ESSENCE, and Pan-STARR1 (Rest et al., 2005; Garg et al., 2007; Mik-

naitis et al., 2007; Rest et al., 2014), to reduce these data. The pipeline performs single-epoch image calibration, including bias subtraction, cross-talk correction, flat-fielding, astrometric calibration, and geometrical distortion correction (using the SWarp software package, Bertin et al., 2002). It performs PSF photometry using a modified version of DoPHOT (Schechter et al., 1993). While the PSF varies across the entire field of view, it is relatively consistent across individual CCDs. Therefore, it is sufficient to calculate a single PSF for each image and CCD to account for image quality variations across the field of view as a function of time. The pipeline then applies quality cuts to the resultant catalogue to remove stars less than 20 pixels from the edges of the CCDs, stars with a significantly brighter neighbour, and stars with photometric errors greater than 3σ (where σ is the mean photometric error of all objects in the corresponding 0.5 mag bin). Given our interest in variable objects, only relative photometry is needed, and we do not perform absolute photometric calibration.

2.2.3 Light Curve Creation

In order to remove the effects of short-term changes in the atmosphere (cloud coverage, haze, etc) and changes in airmass, we select ten bright, unsaturated, non-variable stars from each CCD to use as reference stars. For each CCD, we shift the light curves of our ten reference stars from that CCD to the same magnitude scale and apply a sigma-clipping algorithm to remove bad points affected by cosmic rays or CCD defects. We create a single reference light curve from the weighted means of the individual light curves. Sigma clipping is only used in the creation of our calibration light curve and is not applied to our sources in any subsequent steps. We then subtract this calibration light curve from every source identified in the corresponding CCD. The error introduced by our calibration procedure is

two orders of magnitude smaller than the overall scatter in the light curves. Note that this process was run separately for each night.

Given that our reference stars are typically redder than white dwarfs, airmass-related effects are still visible in the light curves of many of our sources; these effects lead to significant peaks in the Fourier Transform, especially around 4 cycles per day (see Section 2.4.1). To remove this effect, we additionally fit a third-order polynomial to the calibrated source light curves.

2.2.4 Optical Spectroscopy

We obtained follow-up optical spectroscopy of two of the variable sources using the Blue Channel Spectrograph on the 6.5m MMT in October 2017. We operated the spectrograph with the 832 line mm^{-1} grating in second order, providing wavelength coverage from 3600 Å to 4500 Å and a spectral resolution of 1.0 Å. We obtained all observations at the parallactic angle, with a comparison lamp exposure paired with every observation. We flux-calibrated using blue spectrophotometric standards (Massey et al., 1988).

We obtained follow-up optical spectroscopy of two additional variable sources using the Gemini Multi-Object Spectrograph on the 8m Gemini South telescope as part of the programme GS-2018A-Q-319. Observations were obtained using the B600 grating and a 1.0 arcsec slit, providing wavelength coverage from 3650 Å to 6750 Å and a spectral resolution of 3.6 Å. Targets were flux-calibrated using the spectrophotometric standard LTT7379.

2.3 Transits

Planetary eclipses around white dwarfs should only last a few min, hence such events would only affect one or two data points per orbital period. Given the

extremely short durations, traditional eclipse search algorithms like the box-least-squares periodogram are not a good way to identify white dwarf transits. Instead, a simple search for 5σ significant dips in flux is sufficient. However, identifying the source of these drop-outs, whether they are intrinsic to the source or not (due to instrumental or sky background problems), can be difficult. Using a 5σ threshold, Fulton et al. (2014) find 11,570 drop-outs (0.27%) out of 4.3 million data points in the Pan-STARRS Medium Deep Field data. However, further inspection of the images with the drop-out points show that none are compatible with eclipses by substellar companions to white dwarfs in those fields.

Figure 2.1 shows the magnitude distribution of the point sources in our first DECam field (top), as well as the standard deviation σ of the light curve of each source as a function of magnitude (bottom). This figure shows that our sample is incomplete beyond $g = 22.5$ mag. The hook feature seen around g=22 mag in the standard deviation plot is due to contamination from barely resolved sources in our sample. Even though the limiting magnitude of the individual DECam images is $g \approx$24 mag, our data reduction pipeline only includes sources that are detected at a signal-to-noise ratio S/N$\geq$10. This S/N ratio enables us to identify eclipses as shallow as 0.5 mag at 5σ confidence level, which is essential for finding Earth-size planets.

There are 31732 detections with point spread functions consistent with point sources in our DECam field. We have a total of 1024 images, which results in more than 30 million data points. We check each light curve for significant ($\geq 5\sigma$) dips and visually inspect the images with potential transits. We find 5244 potential transits, a significantly smaller fraction compared to the Fulton et al. (2014) study. However, our imaging pipeline already removes most sources near the edges and near bright, saturated stars. Visual inspection of these dips shows that the majority of these sources are either close to the edge of the chip, near

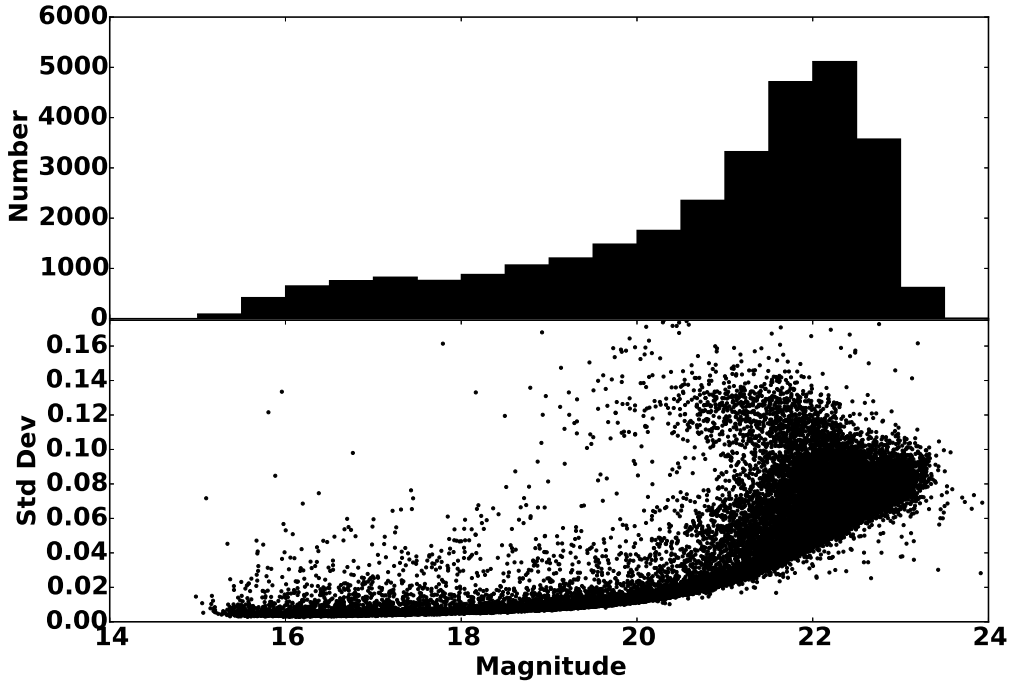

Fig. 2.1.— Magnitude distribution (top) and plot of standard deviation (bottom) of the light curve as a function of magnitude for the point sources included in our analysis. The hook feature seen in the standard deviation plot around g=22 mag is due to contamination from barely resolved sources.

bad pixels, or elongated, and are thus also not real. The point spread function is worse near the edges of the DECam field of view and it gets worse at high airmass (toward the end of the night). This explains many of the elongated images, which result in a lower flux measurement in our photometry.

Of our 5244 potential transits, we find eight that appear to be real, though interestingly, no source exhibits more than one genuine drop-out. However, even with a 5σ threshhold and assuming gaussian errors, we still expect $\approx$18 such deviations in a sample of 30 million points simply due to random scatter. Hence, we expect to find about nine 5σ drop-outs. To determine whether these eight drop-outs are real, we visually inspect difference images obtained with High Order Transform of PSF and Template Subtraction (HOTPANTS, Becker, 2015). Figure 2.2 shows the image and difference image of an example drop-out candidate. We observe no corresponding dip in the difference images for our drop-out candidate, although it should be noted that for five of our eight drop-outs, the star is poorly subtracted. Therefore, while we do find eight dips consistent with a planetary transit of a white dwarf in our photometry, none of these dips appear significant to 3σ in the difference images so they are likely not real.

Of our 31732 targets, only 5011 are detected in *Gaia* Data Release 2 (Gaia Collaboration et al., 2018) with parallax over error ≥ 4, and so *Gaia* is not useful for estimating the total number of white dwarfs in our field at these faint magnitudes. However, the Besançon Galaxy model (Robin et al., 2003) predicts 30381 stars with $13 \leq g \leq 24$ in our field, in good agreement with our 31732 detections. The model also predicts 374 white dwarfs within our field, giving a WD fraction of 1.23%. Belardi et al. (2016) calculated an expected detection rate of 0.7% due to the observing window from the ground for orbital periods less than 30 h. Therefore, based on these numbers, we would expect to find 2.6 planets in our sample if every white dwarf had an earth-mass planetary companion in its

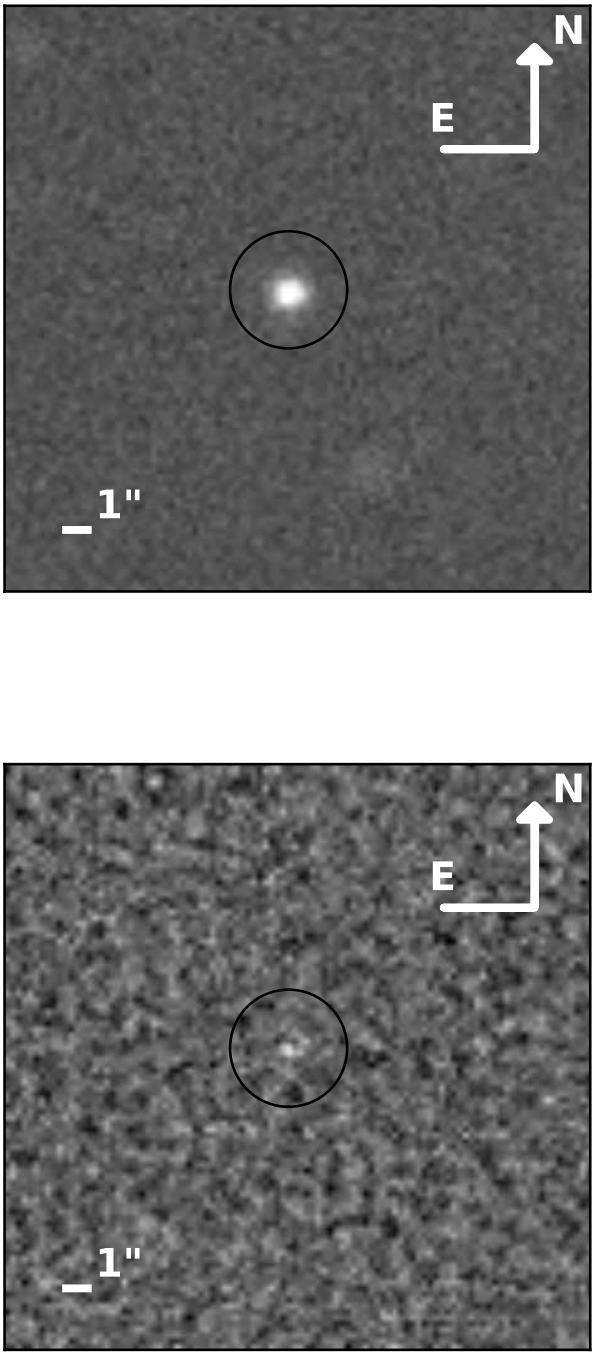

Fig. 2.2.— Image taken on UT 2014 Feb 05 at 05:21:18, corresponding to the drop-out candidate at RA = 09:07:10 and Dec = -04:29:44 (top) and the difference image (bottom). The target is circled.

habitable zone.

2.4 Variability

2.4.1 Variable Candidate Selection

Using the VARTOOLS suite of software (Hartman & Bakos, 2016), we run a Lomb-Scargle periodogram analysis on all the sources in the field. From this, we get the five most significant peaks in the periodogram and their corresponding false alarm probability (FAP). Figure 2.3 shows the distribution of log_{10}(FAP) values as a function of period for our sample. In theory, a star with $log_{10}(\text{FAP}) = -6.2$ has a probability of being a variable object at the 5σ confidence level, with values more negative having higher probability of real variability. We use this limit to select our initial variable candidates. However, as discussed in Macfarlane et al. (2015), the 5σ confidence level can be more negative for real data than the theoretical limit due to systematic effects such as red noise, which introduces a larger spread in log_{10}(FAP) values at longer periods.

Of our 31732 sources, we find 889 variable candidates with at least one period with $log_{10}(\text{FAP}) \leq -6.2$. However, as mentioned above, this is only a theoretical limit, and we expect the real 5σ confidence level to be more negative, especially at longer periods. Therefore, we use the Period04 package (Lenz & Breger, 2014) to inspect each candidate. We compare the amplitudes of the observed peaks with the median amplitude, $\langle \text{A} \rangle$, of the Fourier Transform and look for significant peaks ($\geq 5\langle \text{A} \rangle$). Of our initial 889 candidates, 213 show no evidence of a significant peak upon inspection with Period04. For the remaining targets, we phase-fold the light curves to the period determined by Period04. Many of the resulting phase-folded light curves exhibit obvious problems due to attempts to fit outliers and minor

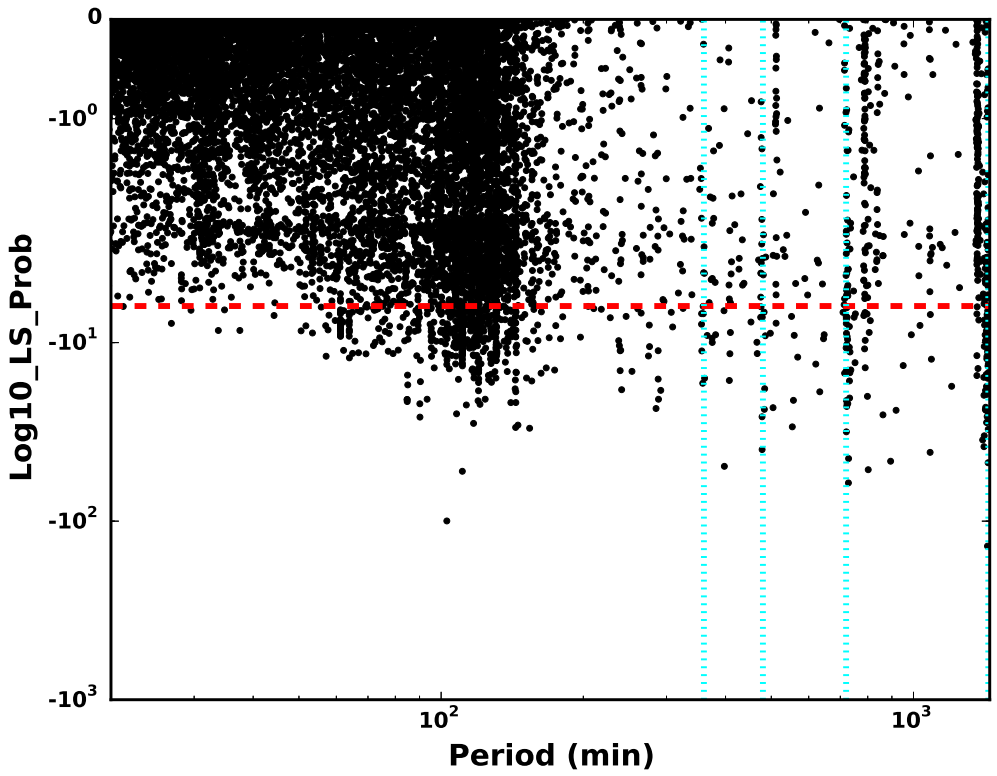

Fig. 2.3.— The false alarm probability ($log_{10}(FAP)$) as a function of period for our sample. The red dashed line shows the theoretical 5σ confidence level; we select all objects below this line as our initial variable candidates. Cyan dotted lines mark periods of 6, 8, 12, and 24 hrs.

zero-point magnitude differences across nights (due to our calibration method). Additionally, we see a significant number of false positives, occurring around 6, 8, 12, and 24 hours (see Fig. 2.3) due to our observing window from the ground. These problems result in poor phase coverage, and the light curves for these objects show no compelling evidence of variation at the periods and amplitudes determined.

However, we find 49 objects that do show genuine variability in their light curves. Table 2.1 presents the coordinates, periods, CFHT Legacy Survey *ugriz* photometry, and variable types for these sources. Note that for some, our method has difficulty finding an accurate period; most of these objects appear to have periods longer than our 4 hour nightly observing window, leading to poor phase coverage (see Section 2.4.3). However, their light curves do exhibit clear variability. For example, J0902−0510, J0903−0516, and J0905−0438 are eclipsing detached binary systems, but our phase coverage is not good enough to recover the binary period.

For the majority of our targets, we are able to determine the type of variable star from the colours, period, and general shape of the light curve. Figure 2.4 shows the colour-colour diagram for our variable targets, separated by type, along with all non-variable objects with $g<20$ in the field, and the predicted colors[a] for pure hydrogen and pure helium white dwarfs (Holberg & Bergeron, 2006; Kowalski & Saumon, 2006; Tremblay et al., 2011; Bergeron et al., 2011). The CFHT Legacy Survey Wide 2 Field has low-extinction, $E(B-V) = 0.02$ mag. Hence, most pulsating stars (δ Scuti and RR Lyrae) cluster around relatively blue colors ($g-r \sim 0$), and are easy to identify, whereas detached and contact binaries involve stars with many different spectral types. Hence, these binaries appear everywhere along the stellar sequence.

[a]http://www.astro.umontreal.ca/ bergeron/CoolingModels/

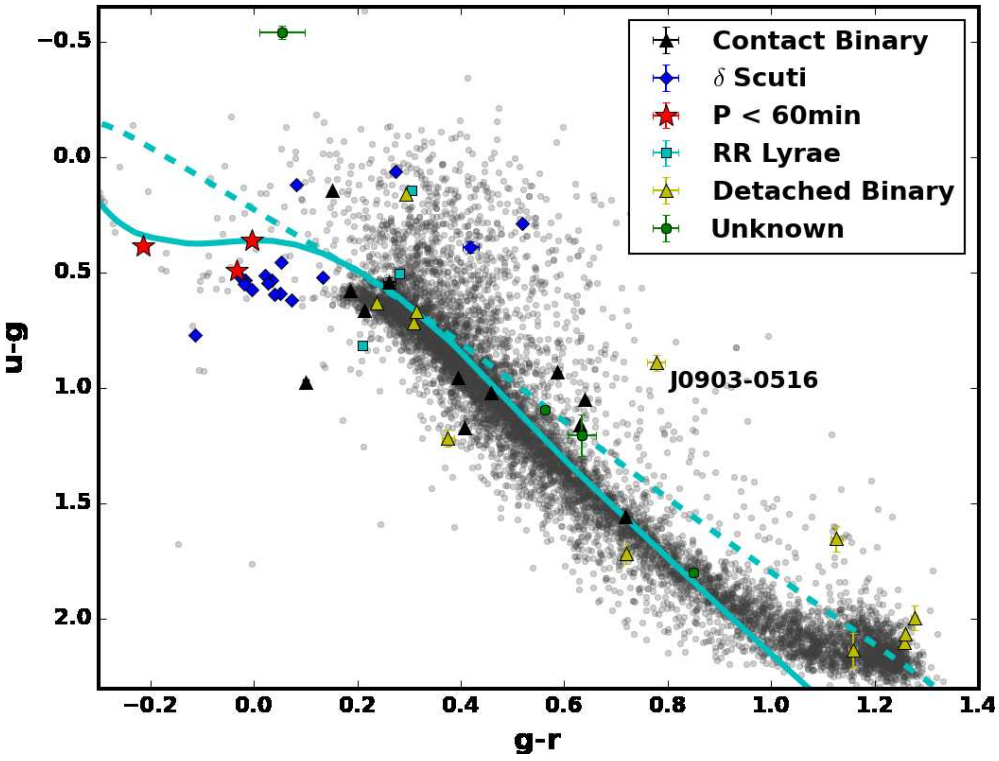

Fig. 2.4.— Colour-colour diagrams for our 49 variable objects and non-variable objects with g<20 mag (grey points). Colors are taken from the CFHT Legacy Survey *ugriz* photometry (AB scale). Predicted colors for log g = 8.0 white dwarfs with pure hydrogen atmospheres (solid line) and pure helium atmospheres (dashed line) are shown for reference. The white dwarf + M dwarf binary J0903−0516 is labelled.

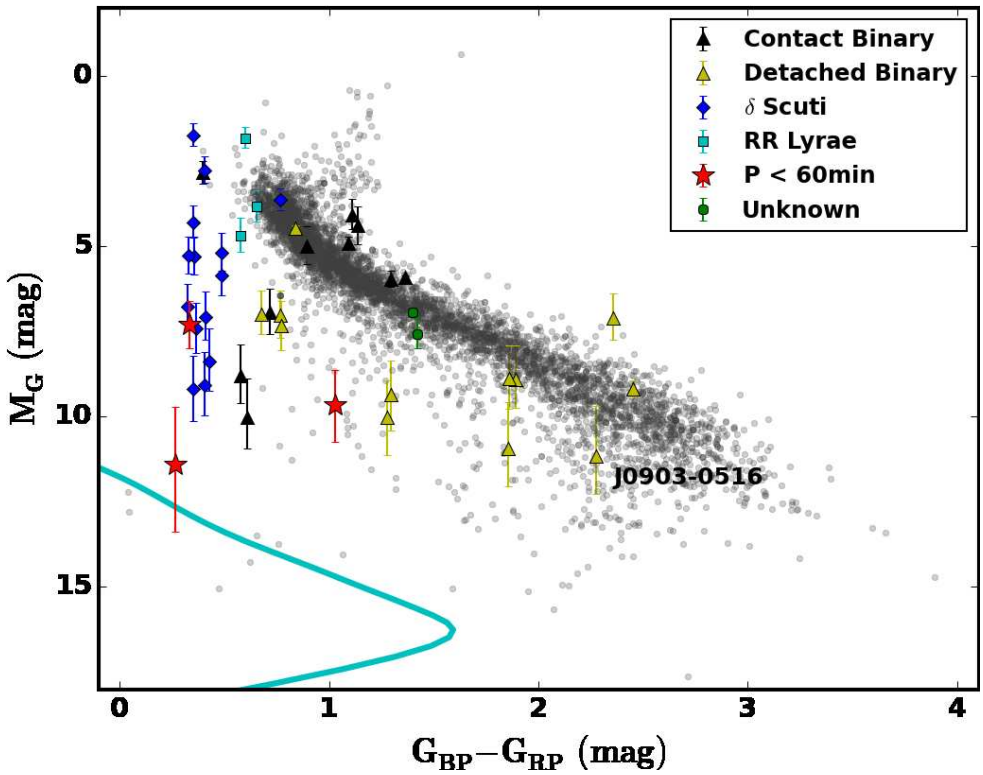

Fig. 2.5.— Colour-magnitude diagram for our 45 variable objects detected with *Gaia*. Symbols are the same as Figure 2.4. The 5001 non-variable sources from our survey with parallax over error ≥ 4 are shown as grey points. The cyan line shows the model sequence for a $0.6M_{\odot}$H atmosphere white dwarf. The white dwarf + M dwarf binary J0903−0516 is labelled.

Additionally, 45 of our variable sources were detected with *Gaia*. However, 11 have negative parallax values and only 10 have parallax over error ≥ 4. We use the geometric distance estimates from Bailer-Jones et al. (2018), inferred from Bayesian analysis with a weak distance prior based on an exponentially decreasing space density such that the probability *P(r—L)*

$$P(r|L) = \begin{cases} \frac{1}{2L^3} r^2 e^{-r/L}, & \text{if } r > 0 \\ 0, & \text{otherwise} \end{cases} \tag{2.1}$$

where r is the distance and $L > 0$ is a scale length.

In Figure 2.5, we show the colour-magnitude diagram for these 45 sources. We also include the 5001 non-variable sources (grey points) detected with *Gaia* with parallax over error ≥ 4 and the model sequence (cyan line) for a $0.6 M_{\odot}$H atmosphere white dwarf. The main sequence is clearly visible, and the positions of our variable sources show good agreement with our classifications.

In the following sections, we discuss our results for each variable type.

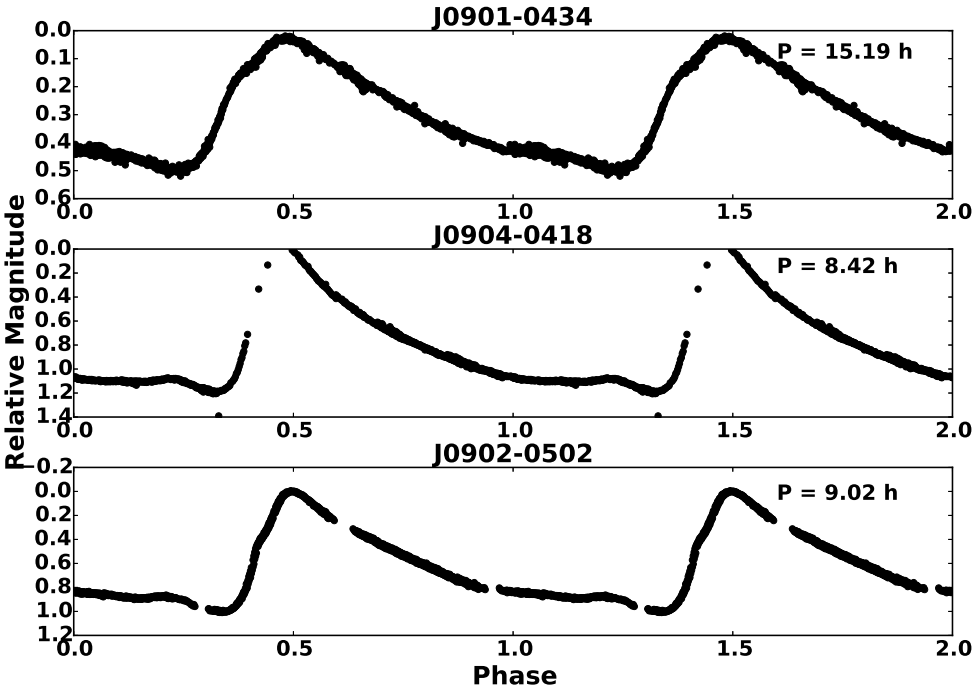

Fig. 2.6.— Phase-folded light curves for the three previously known RR Lyrae variables.

Table 2.1. Variable objects from first field.

Object	RA	Dec	Period (hr)	u	g	r	i	z	Type
$J0859-0439$	08:59:37.250	−04:39:29.27	7.21	22.79	21.07	20.35	19.74	19.63	Detached
$J0900-0426$	09:00:20.133	−04:26:27.36	46.15	22.43	21.21	20.84	20.21	20.30	Detached
$J0901-0350$ [c]	09:01:03.319	−03:50:42.54	6.80	16.96	15.91	15.27	14.94	14.39	Contact
$J0901-0351$	09:01:23.589	−03:51:06.45	21.82	19.66	18.94	18.63	18.51	18.52	Detached
$J0901-0352$	09:01:29.915	−03:52:34.44	7.19	21.76	21.22	20.95	20.92	20.90	Contact
$J0901-0525$	09:01:38.071	−05:25:05.08	96.00	19.16	18.53	18.29	18.21	18.48	Detached
$J0901-0457$	09:01:56.909	−04:57:04.07	6.96	19.99	19.33	19.11	18.96	18.92	Contact
$J0902-0422$	09:02:21.571	−04:22:42.30	60.00	22.78	20.79	19.51	18.65	18.41	Detached
$J0902-0439$	09:02:45.974	−04:39:34.64	7.08	21.04	20.07	19.97	19.83	19.64	Contact
$J0902-0353$ [c]	09:02:48.028	−03:53:03.22	7.60	18.10	16.93	16.52	16.51	15.91	Contact
$J0902-0510$	09:02:57.061	−05:10:20.81	...	20.20	19.53	19.22	19.10	19.23	Detached
$J0903-0516$	09:03:24.589	−05:16:53.25	...	22.72	21.83	21.05	19.70	19.10	Detached
$J0903-0429$	09:03:42.089	−04:29:40.20	6.09	23.10	21.96	19.80	18.97	18.63	Detached
$J0903-0448$	09:03:44.624	−04:48:32.97	14.04	21.91	19.81	18.55	17.40	16.96	Detached
$J0904-0415$ [c]	09:04:07.252	−04:15:53.13	6.08	18.82	17.26	16.55	16.75	16.18	Contact
$J0904-0438$	09:04:15.549	−04:38:03.73	6.22	18.80	17.64	17.01	17.07	16.62	Contact
$J0904-0429$	09:04:31.582	−04:29:29.13	8.89	17.51	16.58	16.00	16.33	15.53	Contact
$J0904-0516$ [c]	09:04:32.882	−05:16:57.97	10.17	15.97	15.82	15.67	15.64	15.65	Contact
$J0904-0404$	09:04:37.052	−04:04:23.43	5.97	20.11	19.53	19.34	19.33	19.34	Contact
$J0904-0450$	09:04:42.776	−04:50:55.14	7.29	20.57	19.55	19.09	19.11	19.11	Contact
$J0905-0520$ [c]	09:05:09.954	−05:20:49.69	28.57	15.75	15.59	15.29	15.18	14.87	Detached
$J0905-0438$	09:05:16.806	−04:38:18.66	...	21.82	19.75	18.50	17.49	16.83	Detached
$J0905-0511$	09:05:49.293	−05:11:46.41	26.09	23.18	21.53	20.40	19.75	19.55	Detached
$J0905-0507$ [c]	09:05:51.584	−05:07:08.31	8.51	18.74	17.78	17.39	17.34	17.25	Contact
Object	RA	Dec	Period	u	g	r	i	z	Type

Table 2.1—Continued

Object	RA	Dec	Period (hr)	u	g	r	i	z	Type
			(hr)						
$J0901-0434$ [b]	09:01:41.200	−04:34:10.06	15.19	18.02	17.21	17.00	16.89	16.89	RR Lyrae
$J0902-0502$ [b]	09:02:22.283	−05:02:01.24	9.02	17.98	17.48	17.20	17.36	17.49	RR Lyrae
$J0904-0418$ [b]	09:04:57.676	−04:18:15.11	8.42	16.00	15.85	15.54	16.02	15.15	RR Lyrae
Object	RA	Dec	Period (min)	u	g	r	i	z	Type
$J0900-0444$	09:00:22.458	−04:44:12.28	69.03	19.76	19.22	19.19	19.23	19.33	δ Scuti
$J0900-0358$	09:00:33.589	−03:58:24.21	91.95	18.72	18.10	18.03	18.03	18.07	δ Scuti
$J0900-0456$	09:00:49.936	−04:56:24.71	73.13	17.62	17.17	17.12	17.18	17.26	δ Scuti
$J0901-0437$	09:01:53.875	−04:37:14.94	96.6	21.93	21.54	21.12	21.06	20.97	δ Scuti
$J0902-0351$	09:02:33.540	−03:51:50.44	93.6	18.42	17.65	17.76	17.65	17.73	δ Scuti
$J0903-0519$	09:03:16.452	−05:19:11.81	55.41	20.55	20.01	20.03	20.08	20.16	δ Scuti
$J0904-0506$	09:04:11.330	−05:06:22.54	59.26	19.58	19.07	19.05	19.10	19.18	δ Scuti
$J0904-0442$	09:04:29.256	−04:42:50.98	67.51	19.30	18.71	18.66	18.74	18.83	δ Scuti
$J0904-0423$	09:04:50.248	−04:23:43.93	57.19	18.16	17.62	17.59	17.79	17.77	δ Scuti
$J0904-0515$	09:04:50.834	−05:15:34.55	91.78	16.25	16.13	16.04	16.08	16.08	δ Scuti
$J0905-0437$	09:05:28.246	−04:37:26.78	67.61	15.78	15.72	15.45	16.15	15.53	δ Scuti
$J0905-0433$	09:05:35.177	−04:33:54.28	56.03	19.24	18.72	18.74	18.86	18.98	δ Scuti
$J0905-0430$	09:05:40.849	−04:30:17.85	59.33	18.48	17.93	17.95	18.03	18.12	δ Scuti
$J0905-0458$	09:05:45.608	−04:58:27.99	59.90	20.20	19.68	19.54	19.77	19.86	δ Scuti
$J0906-0407$	09:06:21.666	−04:07:23.86	15.02	16.81	16.52	16.00	16.46	15.70	δ Scuti
$J0904-0532$	09:04:15.727	−05:32:47.04	45.34	19.79	19.30	19.33	19.43	19.51	δ Scuti
			24.21						
Object	RA	Dec	Period (min)	u	g	r	i	z	Type

Table 2.1—Continued

Object	RA	Dec	Period (hr)	u	g	r	i	z	Type
$J0859-0429$	08:59:27.222	−04:29:16.34	7.76 5.30	20.93	20.54	20.76	20.91	21.06	ZZ Ceti
$J0900-0442$ [a]	09:00:51.516	−04:42:49.18	14.46 12.62	20.97	20.60	20.61	20.11	19.67	ZZ Ceti
Object	RA	Dec	Period (min)	u	g	r	i	z	Type
$J0900-0352$	09:00:53.225	−03:52:03.96	162.90	23.51	22.30	21.67	21.41	21.28	...
$J0902-0502$	09:02:46.931	−05:02:45.10	...	16.98	15.89	15.33	15.16	14.71	...
$J0904-0516$	09:04:02.124	−05:16:45.78	454.26 83.38	21.90	22.44	22.39	22.72	22.18	... ...
$J0905-0511$	09:05:08.181	−05:11:26.75	106.67	20.24	18.43	17.58	17.21	17.04	...

Note. — Coordinates, periods, *ugriz* photometry from the CFHT Legacy Survey, and determined variable type for out 49 variable candidates. Sources for previously known variables are provided.

Note. — *a*: Belardi et al. (2016), *b*: Drake et al. (2013), *c*: Drake et al. (2014).

2.4.2 RR Lyrae

There are three previously known RR Lyrae in our field that were identified as part of the Catalina survey (Drake et al., 2013, 2014). Figure 2.6 shows the phase-folded light curves for these objects. They display $\geq$ 0.5 mag variations with periods ranging from 8 to 15 h. We recover, and independently confirm, the pulsation periods of these three objects in our DECam data. Our phase-coverage for all three pulsators is excellent, demonstrating that we are able to identify variable stars at hour and $\sim$day long periods. We do not find any additional RR Lyrae in this field.

2.4.3 Contact and Detached Binaries

There are six previously known contact and detached binaries in our field that were identified by Drake et al. (2014). Figure 2.7 shows the phase-folded light curves for three of these objects. They display $\geq$0.15 mag variations with binary periods ranging from 6.1 to 28.6 h. Again, our phase coverage is excellent, and our observations cover $> 90\%$ of the binary orbit even for the longest period binary in this sample, J0905$-$0520 with $P = 28.6$ h.

We identified an additional set of 18 new binary systems with our DECam data; 7 contact binaries and 11 detached binaries; these are shown in Figure 2.4 as black and yellow triangles respectively. Figure 2.8 shows example phase-folded light curves for four of our new contact and detached binary systems. The contact binaries have periods ranging from 6 to 9 hours, while the detached binaries have periods covering a much wider range, from 6 h to 4 days. However, for five of our 11 detached binaries, the periods are poorly constrained, and for another three, we could not determine a period at all. As mentioned above, this is likely due to poor phase coverage for longer orbital periods. For six of our 11 detached binaries,

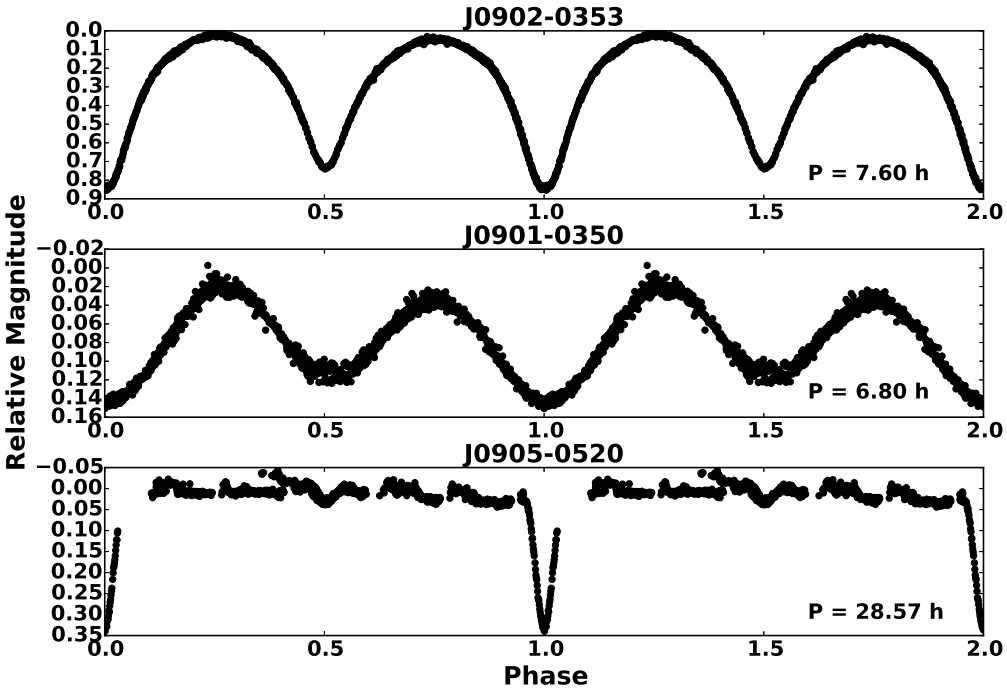

Fig. 2.7.— Phase-folded light curves for two previously identified contact binaries (top panels) and a detached binary (bottom panel) from Drake et al. (2014).

we observe only one or two transits over the entire eight half-nights (see Fig. 2.8); in comparison, our contact binaries have periods short enough to observe a transit every half-night, allowing for much better constraints on their orbital periods.

One of the new detached binaries involves an eclipsing compact object. Figure 2.9 shows our light curve for J0903−0516. We observe only a single transit, so we cannot determine a period. However, the short (≈ 30 min) duration and the sharp ingress and egress of the transit mark this object as a white dwarf + M dwarf binary. The observed light curve is essentially identical to the other eclipsing white dwarf + M dwarf binaries known (e.g., Parsons et al., 2017). About 22% of field white dwarfs have late-type stellar companions (Farihi et al., 2005), while 3.4% of these systems are eclipsing with $P < 2$ day orbits (Parsons et al., 2013). Hence, the frequency of eclipsing white dwarf + M dwarf binaries is likely around 0.75% for randomly oriented orbits. Given the predicted number of white dwarfs from the Besancon Galaxy model (see §4), we would expect to find up to 3 eclipsing white dwarf + M dwarfs in our dataset. Hence, the discovery of such a system in our survey is not surprising.

2.4.4 δ Scuti Type Pulsators

δ Scuti stars are the second most common type of variable stars in our survey. They typically have A-F spectral types and pulsation periods of 0.48-6 hrs (Chang et al., 2013). We find 15 objects with colours and periods consistent with δ Scuti type pulsators. These objects are shown as blue diamonds in Figure 2.4. We show the phase-folded light curves for two of the newly identified δ Scuti type pulsators with periods near 1.6 h in Figure 2.10, and the light curves for a sample of the remaining from a single night in Figure 2.11.

All but one of these pulsators have periods ranging from 55 min to 97 min.

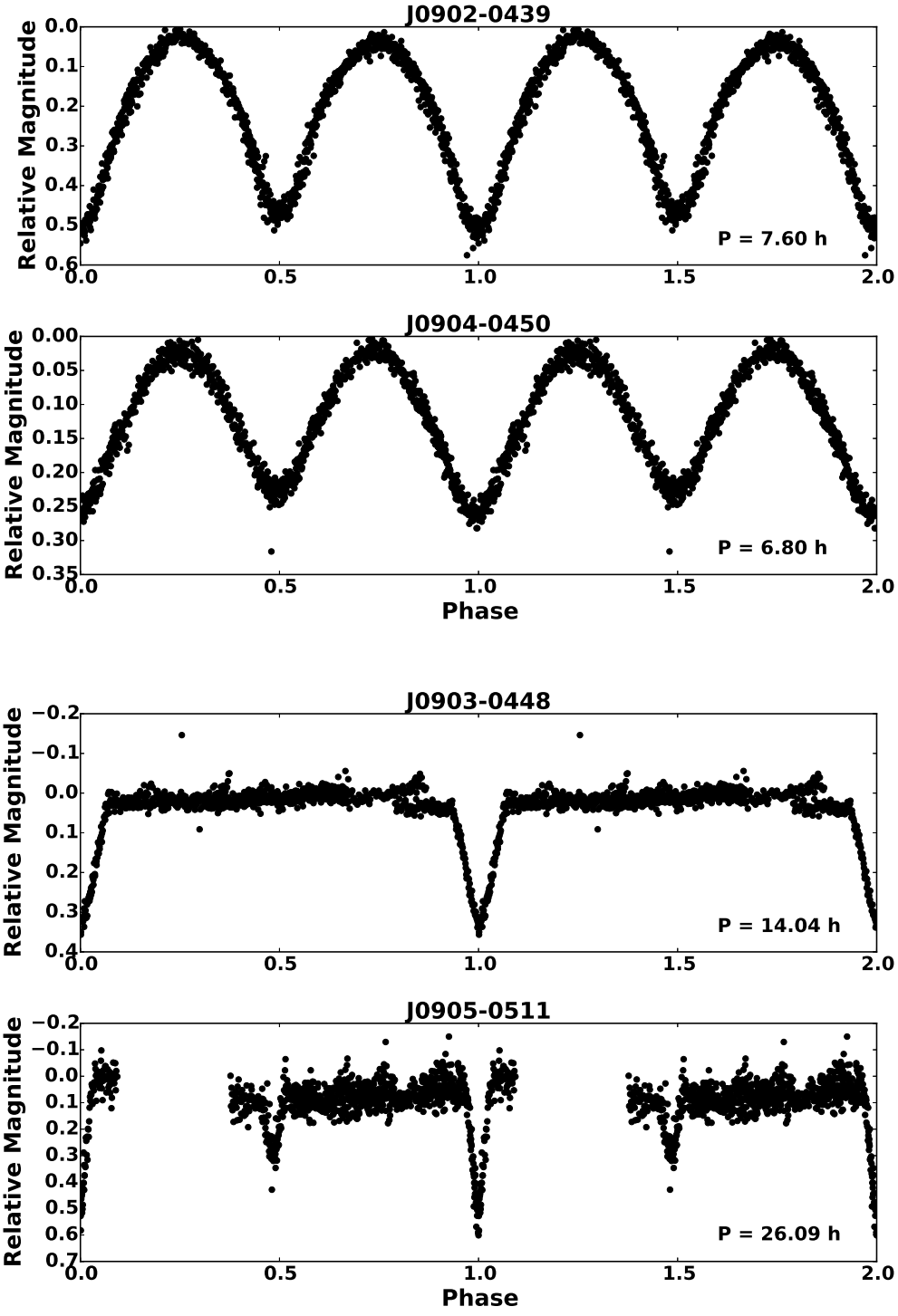

Fig. 2.8.— Representative phase-folded light curves for four of our new contact (top panels) and detached (bottom panels) binaries.

However, there is a relatively red object, J0906-0407 with $g - r = 0.52$ mag, that shows variations with a dominant period of 15 min, which is near the period minimum of ≈18 min observed in the Kepler mission δ Scuti star sample (Uytterhoeven et al., 2011).

Given the relatively short period that could either indicate a pulsating ZZ Ceti white dwarf or a short period δ Scuti, we obtained follow-up spectroscopy of J0906-0407 to constrain its nature. Figure 2.12 shows its optical spectrum, which reveals strong Ca II H & K lines and the G-band absorption, as well as relatively weak Hδ and Hγ lines. Hence, J0906-0407 is clearly a G star. We compare the equivalent width measurements of these features to the spectral templates from Pickles (1998) and identify this object as a ≈G0V star. Macfarlane et al. (2017) identify two δ Scuti pulsators with dominant periods of 9.0-9.6 min, including the G5 type star OW J075531.59-315058.2. Hence, J0906-0407 appears to be similar to other G-type δ Scuti stars with relatively short pulsation periods.

2.4.5 Short Period Pulsators

Among the 7 objects that cannot be readily identified by colour and period, we find three blue objects with short periods (P < 60 min). Their location in the $u - g$ versus $g - r$ color-color diagram (see Figure 2.4) is consistent with DA white dwarfs. Figure 2.13 shows the light curves and their Fourier transforms for two of these objects. The first is J0900-0442, the ZZ Ceti candidate previously discovered in Belardi et al. (2016) through its high proper motion. We detect two significant periods at 14.46 and 12.62 min, consistent with those found previously. Additionally, we find a second ZZ Ceti candidate in the field. J0859-0429 exhibits significant variations at 7.76 and 5.30 min, consistent with pulsation periods observed in other ZZ Ceti white dwarfs (Fontaine & Brassard, 2008; Winget

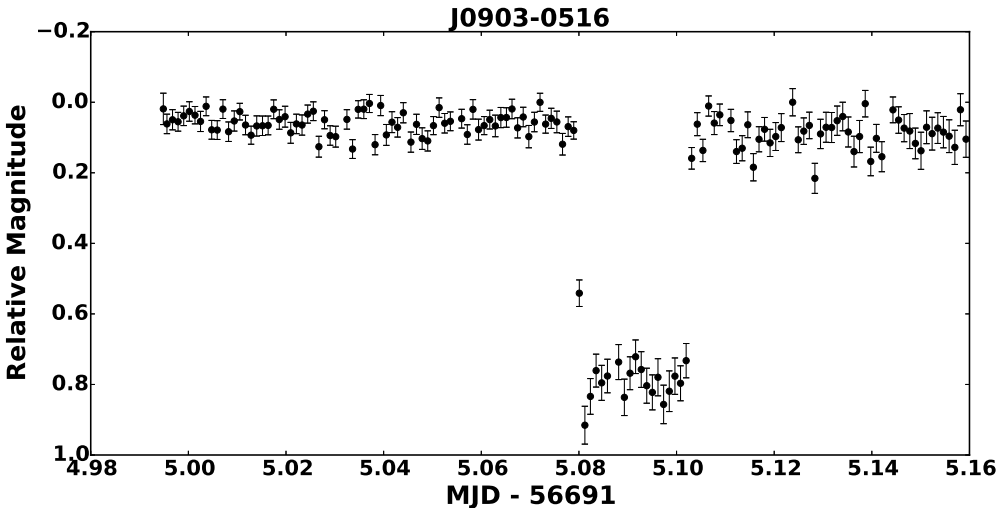

Fig. 2.9.— The single observed transit for the white dwarf + M dwarf binary J0903-0516.

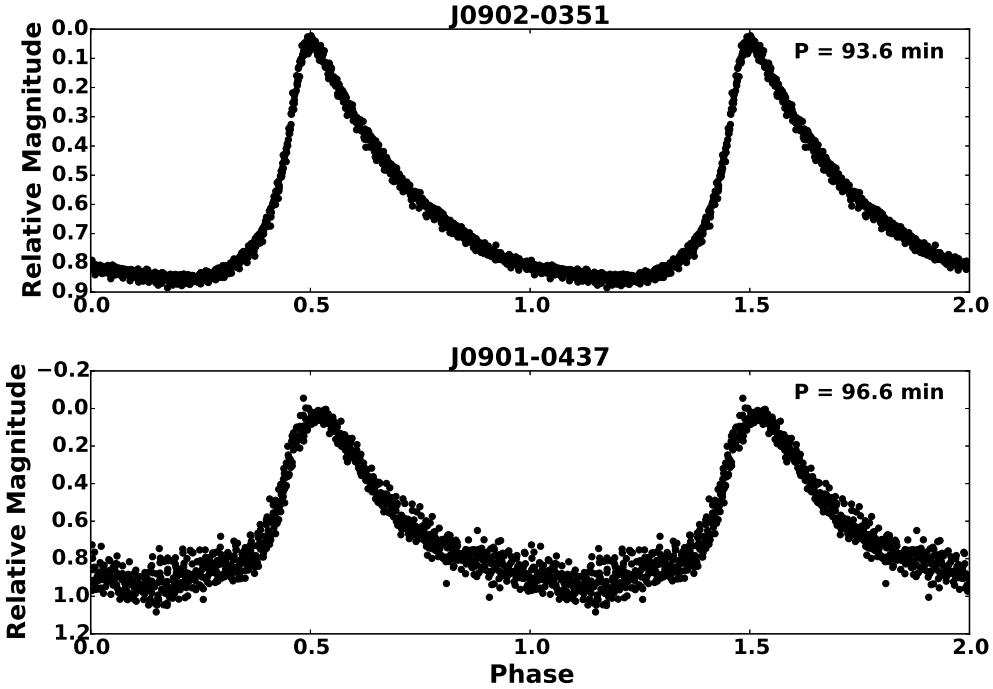

Fig. 2.10.— Phase-folded light curves for two of the newly identified δ Scuti type pulsators.

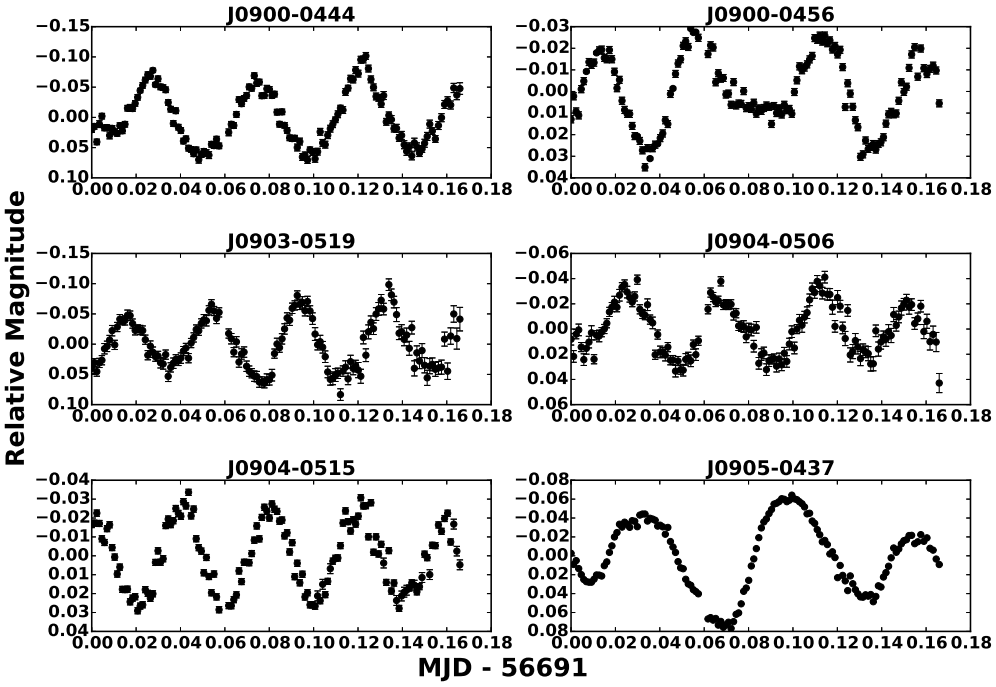

Fig. 2.11.— Light curves from a single night for 6 additional δ Scuti type pulsators in our DECam field.

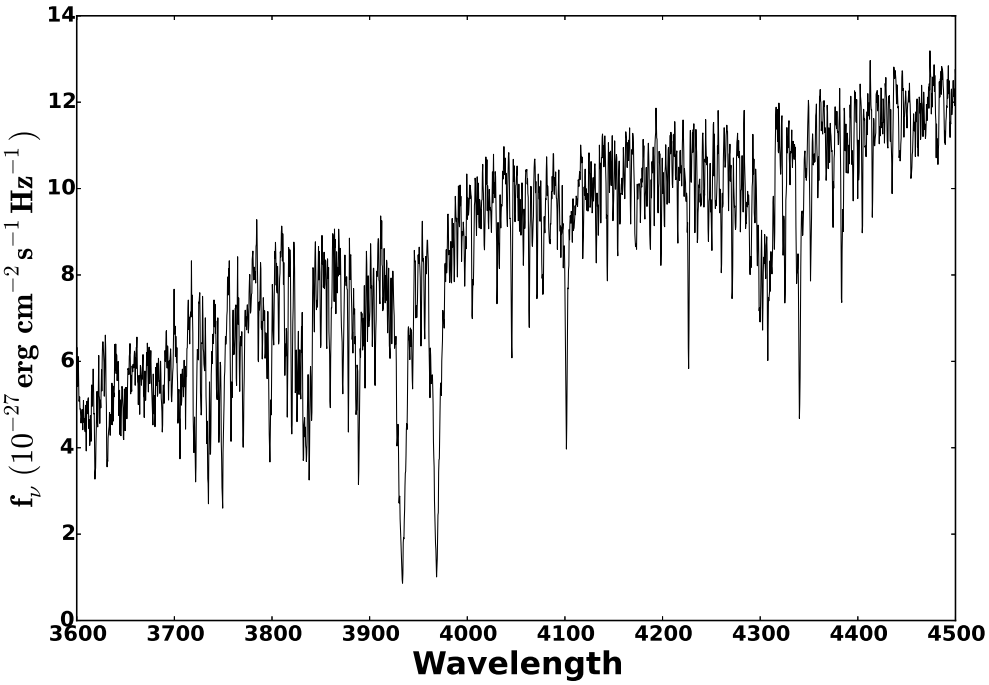

Fig. 2.12.— MMT spectrum of J0906-0407, a newly identified G-type δ Scuti pulsator.

& Kepler, 2008).

J0859-0429 has *ugriz* photometry that puts it right in the middle of the ZZ Ceti instability strip for white dwarfs (Gianninas et al., 2011) and J0900-0442 displays a proper motion of 27 mas yr^{-1} which puts it right in the middle of the white dwarf sequence in the reduced proper motion diagram (Belardi et al., 2016). As discussed in Belardi et al. (2016), the inability of the models to reproduce the SED of J0900-0442 may be due to an unseen companion. The remaining blue object that shows short period pulsations (at 24.21 and 45.34 min), J0904-0532, has colours consistent with a white dwarf, and its spectral energy distribution is well fit by a ≈8600 K object. These pulsation periods are longer than expected and the temperature is cooler than expected for average mass ZZ Ceti white dwarfs.

We obtained follow-up optical spectra of J0859-0429 and J0900-0442 from Gemini South, and J0904-0532 from MMT. The observed line profiles(black) and 1D model fits (red, Gianninas et al., 2011) are shown in Figure 2.14.

The normalised Balmer line profiles of J0859-0429 are best-fit by a pure H atmosphere model with $T_{\mathrm{eff}} = 12940 \pm 690$ K and $\log g = 7.94 \pm 0.15$. These values are consistent with the instability strip for white dwarfs, confirming that J0859-0429 is a ZZ Ceti. Inclusion of Hβ in the fit yields $T_{\mathrm{eff}} = 12400 \pm 410$ K and $\log g = 7.82 \pm 0.15$; the results are consistent within 1σ.

The normalised Balmer line profiles of J0900-0442 are best-fit by a pure H atmosphere model with $T_{\mathrm{eff}} \sim 12140$ K and $\log g \sim 6.85$. These values are broadly consistent with the instability strip; however, the errors are too large to unequivocally confirm that J0900-0442 is a ZZ Ceti. Since the SED of J0900-0442 shows contamination from a late type star, we do not include Hβ in the fit.

The normalised Balmer line profiles of J0904-0532 are best-fit by a pure H atmosphere model with $T_{\mathrm{eff}} = 8350 \pm 80$ K and $\log g = 5.46 \pm 0.16$. Fitting

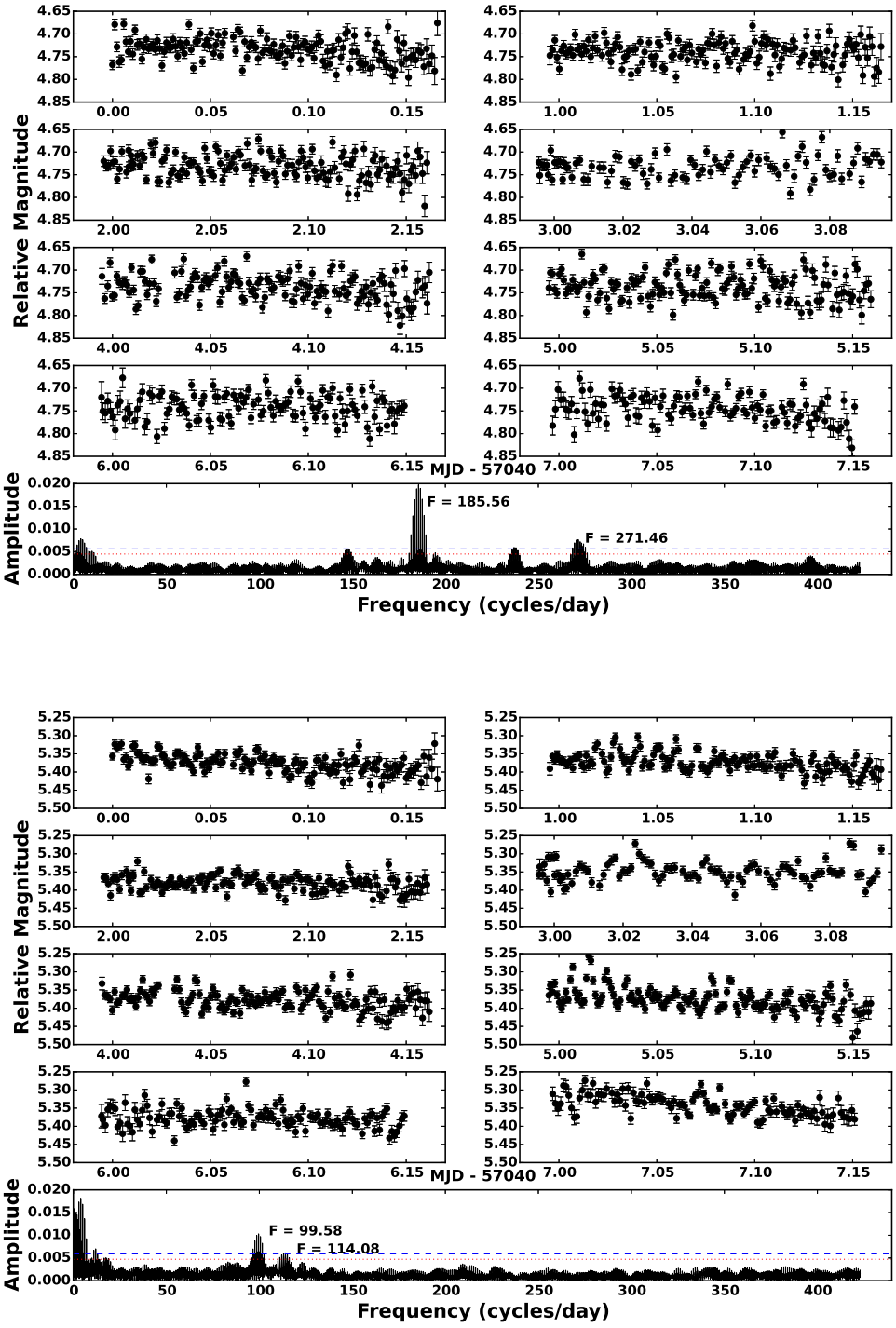

Fig. 2.13.— Light curves (top panels) and Fourier transforms (bottom panel) for J0859-0429 (top) and J0900-0442 (bottom). The red dotted line and blue dashed line in the Fourier transform show, respectively, the $4\langle A\rangle$ and $5\langle A\rangle$ detection limits, where $\langle A\rangle$ the median amplitude of the Fourier transform.

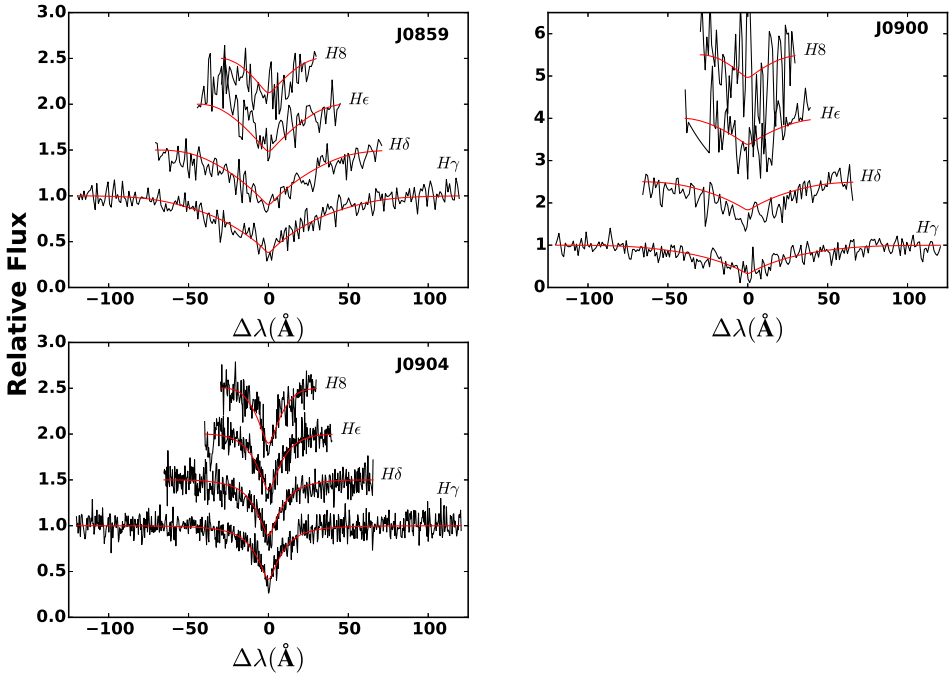

Fig. 2.14.— 1D model fits (red) to the observed Balmer line profiles (black) for J0859-0429 (top left), J0900-0442 (top right), and J0904-0532 (bottom left). For clarity, line profiles are vertically offset from each other.

synthetic main-sequence star spectra with pure H atmosphere white dwarf models, Brown et al. (2017) demonstrate that these models systematically overestimate the surface gravity below 9000 K (Pelisoli et al., 2018). For example, the synthetic spectrum of a main-sequence star with [Fe/H] $= -1$, $T_{\rm eff} = 8000$ K, and $\log g = 4.5$ is best-fit by a white dwarf model with $\log g \approx 5.1$. Hence, the model atmosphere fit is likely an overestimate of the actual surface gravity of this star. Additionally, its position in Figure 2.5 places it in the middle of the 15 δ Scuti type pulsators. Hence, J0904-0532 is certainly a δ Scuti type variable star.

2.4.6 Variables with Undetermined Types

There remains four objects for which we cannot determine the source of variability from colour and period alone. These objects are listed at the bottom of Table 1 and are marked by green circles in Figure 2.4. J0900-0352, J0902-0502, and J0905-0511 have colours consistent with main-sequence stars, but the light curves are simply too inconclusive to make a definitive identification. J0904-0516 has colours consistent with quasars; however, it exhibits variations with periods of 454.26 and 83.38 min, far shorter than the typical periods previously observed in quasars. Follow-up spectroscopy would be helpful in revealing the nature of these four objects, though two of them are relatively faint with $g > 22$ mag.

2.5 Conclusions

We present final results from the first field of the DECam minute-cadence survey. We construct light curves for the 31732 point sources in the field, allowing us to search for potential planetary transits around otherwise difficult to identify low proper motion white dwarfs ($\mu < 20$ mas yr^{-1}). While we find no compelling evidence of such a transit around a white dwarf, we do identify 40 new variable

objects: 18 binary systems (including a white dwarf + M dwarf binary), 16 δ Scuti type pulsators, and two ZZ Ceti white dwarfs. The remaining variable objects of undetermined type will require follow-up spectroscopic observations for reliable classification.

Analysis of the second and third fields is underway and will be presented in a future publication. We expect similar numbers of white dwarfs in the remaining two fields, allowing us to place stringent constraints on the frequency of Earth-sized planets in the habitable zone of white dwarfs. Additionally, surveys like SuperWASP, the Next-Generation Transit Survey, the Transiting Exoplanet Survey Satellite, and ZTF will obtain high-cadence observations for millions of stars. These observations will allow us to probe the variability of the night sky on timescales that remain largely unstudied, and open the possibility of observing previously unknown phenomena.

Acknowledgements

We thank the referee for their helpful suggestions. This work is in part supported by NASA under grant NNX14AF65G. Based on observations at Cerro Tololo Inter-American Observatory, National Optical Astronomy Observatory (NOAO Prop. ID:2014A-0073 and PI: M. Kilic), which is operated by the Association of Universities for Research in Astronomy (AURA) under a cooperative agreement with the National Science Foundation.

This project used data obtained with the Dark Energy Camera (DECam), which was constructed by the Dark Energy Survey (DES) collaboration. Funding for the DES Projects has been provided by the DOE and NSF (USA), MISE (Spain), STFC (UK), HEFCE (UK). NCSA (UIUC), KICP (U. Chicago), CCAPP (Ohio State), MIFPA (Texas A&M), CNPQ, FAPERJ, FINEP (Brazil), MINECO

(Spain), DFG (Germany) and the collaborating institutions in the Dark Energy Survey, which are Argonne Lab, UC Santa Cruz, University of Cambridge, CIEMAT-Madrid, University of Chicago, University College London, DES-Brazil Consortium, University of Edinburgh, ETH Zurich, Fermilab, University of Illinois, ICE (IEEC-CSIC), IFAE Barcelona, Lawrence Berkeley Lab, LMU Munchen and the associated Excellence Cluster Universe, University of Michigan, NOAO, University of Nottingham, Ohio State University, University of Pennsylvania, University of Portsmouth, SLAC National Lab, Stanford University, University of Sussex, and Texas A&M University.

Chapter 3

The DECam Minute Cadence Survey III: New Constraints on the Occurrence Rate of Planetary Companions Around White Dwarfs

3.1 Introduction

The fate of planetary systems as their host stars evolve has long been an outstanding question in astronomy. Current theories of stellar evolution predict that such systems should be disrupted as their host star evolves off the main sequence, destroying close-in planets and moving more distant planets even further out. However, indirect evidence, such as the existence of debris discs around $1.5^{+1.5}_{-0.5}$% of white dwarfs (Wilson et al., 2019) and observations of metal pollution in the atmospheres of 25-50% of white dwarfs (Koester et al., 2014), suggest that something must survive the evolutionary process. Even more suggestive was the discovery of a disintegrating asteroid around the dusty white dwarf WD 1145+017 in long-cadence data from the Kepler/K2 mission (Vanderburg et al., 2015; Gänsicke et al., 2016; Rappaport et al., 2016). Such planetesimals had never been found around white dwarfs previously due to a lack of extended duration high-cadence observations of a large number of white dwarfs. Recently, Manser et al. (2019) found evidence in short cadence spectroscopy of variation in the Ca II triplet caused by a solid-body planetesimal orbiting the white dwarf SDSS J1228+1040, speculated to be the leftover core of a planet.

However, though the vast majority of stars in our galaxy will one day become white dwarfs, there are currently no white dwarfs known to host a solid body

planetary companion. Fulton et al. (2014) used the Pan-STARRS data of ~ 1700 photometrically selected candidates to constrain the frequency of gas giant planets orbiting white dwarfs just outside the Roche limit (0.01 AU) to $< 0.5\%$, but their cadence and sensitivity were not high enough to constrain the frequency of Earth-size planets at the same orbital separation. Van Sluijs & Van Eylen (2018) used long and short cadence K2 data from 1148 confirmed and high-probabality white dwarfs to constrain the frequency of Earth-sized planets in the habitable zone around white dwarfs to $< 28\%$. Rowan et al. (2019) used *GALEX* observations of over 23,000 known and candidate white dwarfs to constrain the occurrence rate of systems analogous to WD 1145+017 to $\leq 0.5\%$ to 3σ, but their results did not consider occurrence rates for habitable Earth-sized planets.

The DECam Minute Cadence Survey (Belardi et al., 2016) was the first high cadence survey of its kind, observing 9 deg^2 of the sky at a cadence of ≈ 90 sec over 8 half-nights per field, specifically looking for planetary transits around a large number of white dwarfs. Analysis of the first 3 deg^2 field found no evidence of planetary transits consistent with a white dwarf but did identify 40 new variable systems, including two new ZZ Ceti pulsators and a new eclipsing white dwarf + M dwarf binary (Belardi et al., 2016; Dame et al., 2019). Here we extract and analyse the photometry for all of the point sources in the remaining two fields to search for transiting and variable objects. We also combine the results from all three fields to calculate constraints on the occurrence rate of habitable zone Earth-sized planets around white dwarfs.

We discuss the details of our observations and reductions in Section 3.2. We discuss the results of our transit search in Section 3.3, present our selection process and list of variable objects in Section 3.4, and conclude in Section 3.5.

3.2 Observations and Data Reduction

3.2.1 DECam Observations

We used the Cerro Tololo Interamerican Observatory 4m telescope equipped with the Dark Energy Camera (DECam) to obtain g-band exposures of nine square degrees, corresponding to three separate pointings (hereafter referred to as fields). During our observing run, two of DECam's 62 CCDs were not functioning, reducing the number of useable CCDs to 60. Each field was observed for eight consecutive half-nights. The first field was centred at RA = 09:03:02 and Dec = -04:35:00 and observed UT 2014 Feb 2-9, the second at RA = 09:03:02 and Dec = -02:23:00 and observed UT 2015 Jan 18-25, and the third at RA = 08:54:14 and Dec = -04:35:00 and observed UT 2015 Feb 8-15. Our DECam fields cover a small portion of the Canada-France-Hawaii Telescope Legacy Survey (CFHTLS) Wide 2 Field, with Megacam *ugriz* photometry available. Exposure times were chosen to obtain S/N $\geq$ 5 photometry of targets brighter than $g = 24.5$ AB mag, giving an overall cadence of $\approx$ 90 s, including the 20 s read-out time of the camera. Results from the first field are discussed in Belardi et al. (2016) and Dame et al. (2019). Here we discuss the results for the remaining two fields.

3.2.2 Photometric Data Reduction

We downloaded the raw DECam data from the NOAO Archive and used the Photpipe pipeline, which was previously used in time-domain surveys like SuperMACHO, ESSENCE, and Pan-STARR1 (Rest et al., 2005; Garg et al., 2007; Miknaitis et al., 2007; Rest et al., 2014), to reduce these data. The pipeline performs single-epoch image calibration, including bias subtraction, cross-talk correction, flat-fielding, astrometric calibration, and geometrical distortion correction (using

the SWarp software package, Bertin et al., 2002). It performs PSF photometry using a modified version of DoPHOT (Schechter et al., 1993), and applies quality cuts to the resultant catalogue to remove stars less than 20 pixels from the edges of the CCDs, stars with a significantly brighter neighbour, and stars with individual photometric point errors greater than 3σ (where σ is the mean photometric point error of all objects in the corresponding 0.5 mag bin). Since the PSF is relatively constant across individual CCDs, it is sufficient to calculate a single PSF for each image and CCD in order to account for image quality variations across the field of view as a function of time. Given our interest in variable objects, only relative photometry is needed, and we do not perform absolute photometric calibration.

3.2.3 Light Curve Creation

In order to remove the effects of short-term changes in the atmosphere (cloud coverage, haze, etc) and changes in airmass, we select ten bright, unsaturated, non-variable stars from each CCD to use as reference stars. For each CCD, we shift the light curves of our ten reference stars from that CCD to the same magnitude scale and apply a sigma-clipping algorithm to remove bad points affected by cosmic rays or CCD defects. We create a single reference light curve from the weighted means of the individual light curves. Sigma clipping is only used in the creation of our calibration light curve and is not applied to our sources in any subsequent steps. We then subtract this calibration light curve from every source identified in the corresponding CCD. The error introduced by our calibration procedure is two orders of magnitude smaller than the overall scatter in the light curves. Note that this process was run separately for each night.

Our reference stars are typically redder than white dwarfs, and airmass-related effects are still visible in the light curves of many of our sources; these effects lead to

significant peaks in the Fourier Transform, especially around 4 cycles per day (see Section 3.4.1). To remove this effect, we additionally fit a third-order polynomial to the calibrated source light curves. The results of our calibration process for a representative source are shown in Figure 3.1. The top panel shows the raw light curve, the middle panel shows the light curve after subtraction of the calibration light curve, and the bottom panel shows the final light curve.

3.3 Transits

3.3.1 Transit Candidates

Any planetary transit of a white dwarf should only last a few minutes, affecting one or two data points per event. The short duration makes these transits difficult to detect via traditional eclipse search algorithms like the box-least-squares periodogram. Instead, we preform a simple search for 5σ dips in flux, where σ is the standard deviation of the light curve. We use the scatter in the light curves as our measure of error because it is the dominant source. We also require that a transit candidate be significant to the 5σ level based on the individual point error of that candidate. This requirement removes potential transits with particularly large individual point errors. This search is sufficient to identify potential white dwarf transits, but it can be difficult to determine if the drop-out is intrinsic to the source or due to instrumental or sky background problems.

We find 3737 potential transits among the 58487 point sources in our DECam fields. We visually inspect images containing drop-out candidates to remove objects near the edge of the chip or bad pixels or that appear elongated in the image. Of our initial 3737 candidates, only 25 pass visual inspection and appear genuine. However, assuming Guassian errors, we still expect to observe ≈ 16 5σ dips in our

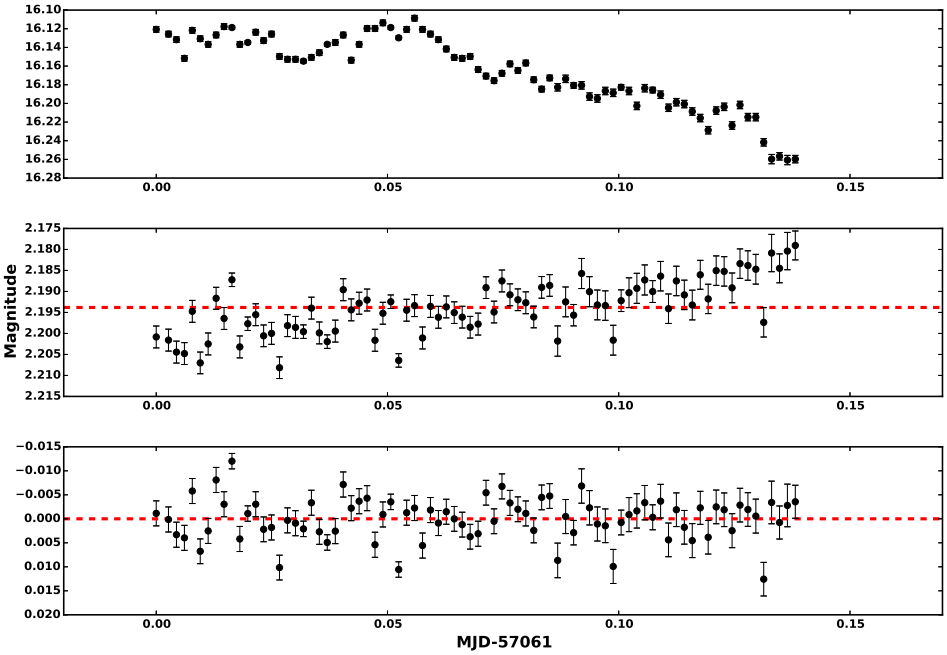

Fig. 3.1.— Raw light curve (top), light curve after subtraction of calibration light curve (middle), and final light curve (bottom) for a representative target. The middle panel shows a clear airmass-related trend not removed by the calibration light curve.

56 million data points. Therefore, we visually inspect difference images created for the remaining 25 candidates using High Order Transform of PSF and Template Subtraction (HOTPANTS) to determine whether these drop-outs are real.

We observe a corresponding dip in the difference image for the drop-out candidate at RA = 08:56:24 and Dec = -04:16:10 (hereafter J0856−0416). Figure 3.2 shows the image and difference image for this candidate. The difference image shows a clear residual. J0856−0416 shows a second 4.6σ drop-out that also shows a clear residual in the corresponding difference image. Therefore, we determine these to be genuine drop-out events. We do not observe corresponding residuals in the 24 other potential transits to 3σ, although it should be noted that for 13 of these candidates, the star is poorly subtracted.

However, while we do observe genuine minute-timescale dips around J0856−0416, it has colors too red to be a white dwarf, and parallax measurements from *Gaia* clearly place it on the main sequence (see Figure 3.6). Additionally, there is no evidence that these dips are periodic in nature. Across eight half-nights, we only observe these two dips $\approx$ 20 min apart. Such brief duration dips around a main sequence star are unexpected and the cause of these dips is beyond the scope of this work. We find no evidence of a drop-out event consistent with a planetary transit of a white dwarf in our photometry.

3.3.2 Constraining Occurrence Rates

The transit of a 0.6 $M_{\odot}$white dwarf by an Earth-sized planet will decrease the observed flux by $\approx 50\%$ (Agol, 2011), allowing us to detect such planets at the 5σ confidence level around white dwarfs with $\sigma \leq 0.15$ mag, where σ is the standard deviation of the light curve. Figure 3.3 shows the magnitude distribution of the point sources in our two fields (top), as well as the standard deviation σ of each

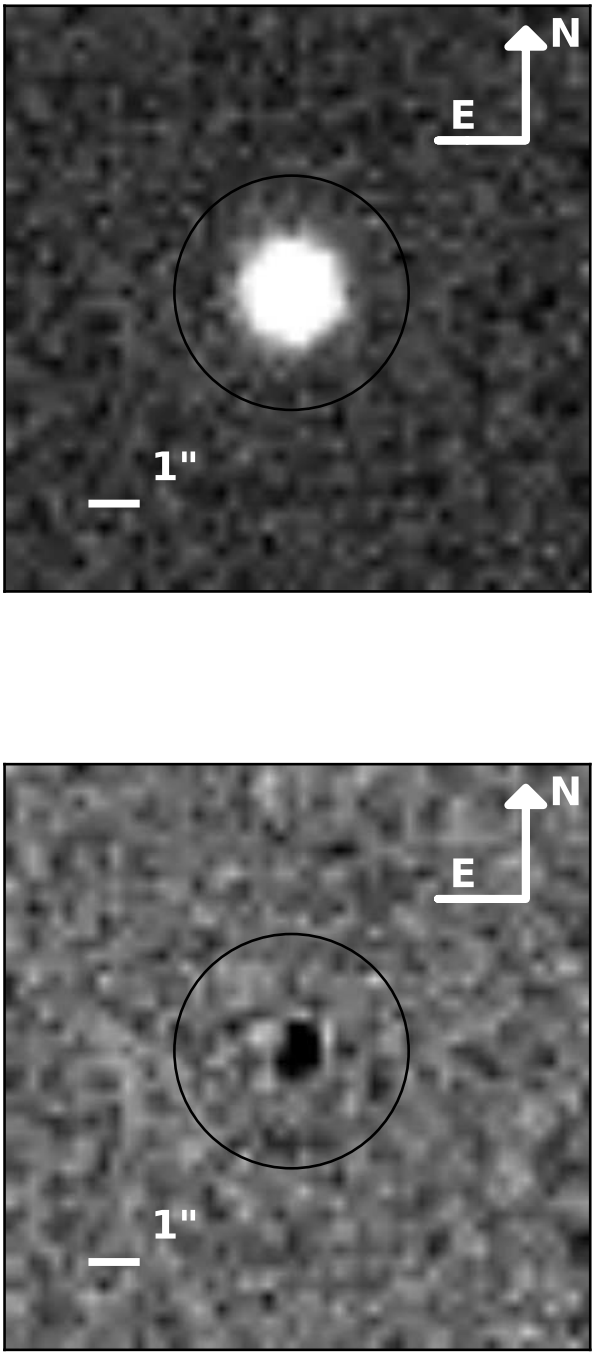

Fig. 3.2.— Image taken on UT 2015 Feb 09 at 05:43:30, corresponding to the drop-out candidate at RA = 08:56:24 and Dec = -04:16:10 (top) and the difference image (bottom). The target is circled. The difference image shows a clear residual.

source as a function of magnitude (bottom). The higher standard deviations for the third field are due to poorer observing conditions. There are 86265 sources in our survey with $\sigma \leq 0.15$ mag. We estimate the white dwarf fraction of 0.98% for our survey based on results from the Besançon Galaxy model[a] We generate simulated catalogues covering 3 deg^2 centred at each field's center using default values. We restrict the simulation to $13 \leq g \leq 24$ for the first and second fields, and $13 \leq g \leq 23$ for the third field to account for the poorer observing conditions. Therefore, we expect 845 white dwarfs in our sample. However, as in our previous work, we observe a hook feature in the plot of standard deviation for objects with $\sigma \geq 0.10$ mag due to contamination from barely resolved sources. Adopting a more conservative threshold of $\sigma \leq 0.10$ mag yields 81835 total sources and 802 estimated white dwarfs.

The probability of finding n planets in a sample of N white dwarfs is given by a Binomial probability distribution

$$P(n; N, f) = \frac{N!}{n!(N-n)!} f^n (1-f)^{N-n}, \tag{3.1}$$

where f is the occurrence rate of planets around white dwarfs. We can constrain the occurrence rate to an interval (f_{min},f_{max}) such that

$$\int_{f_{min}}^{f_{max}} (N+1)^{-1} P(n; N, f) = C \tag{3.2}$$

where C is the desired confidence level and $(N+1)^{-1}$ is a normalization constant. For n=0, we set f_{min}=0 and Equation **3.2** reduces to

$$\int_{0}^{f_{max}} (N+1)^{-1} (1-f)^N = 1 - (1-f_{max})^{N+1} = C. \tag{3.3}$$

[a]The model is available at: https://model.obs-besancon.fr/modele_home.php.

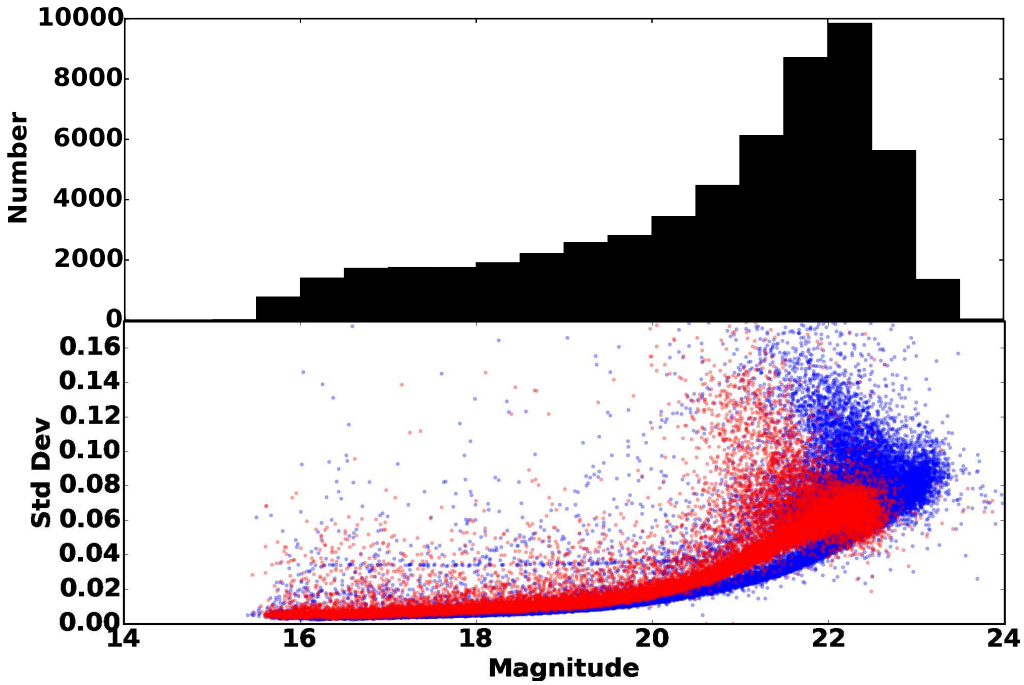

Fig. 3.3.— Magnitude distribution (top) and plot of standard deviation (bottom) of the light curve as a function of magnitude for the point sources included in our analysis. Blue and red points represent the second and third fields, respectively. The higher standard deviations for sources in the third field are due to poorer observing conditions. The hook feature seen in the standard deviation plot around g=22 mag is due to contamination from barely resolved sources.

Solving for f_{max},

$$f_{max} = 1 - (1 - C)^{\frac{1}{N+1}}. \quad (\mathbf{3.4})$$

However, not every planet is detectable, and we must replace N with an effective sample size N' such that

$$N' = P_{trans} P_{det} N \quad (\mathbf{3.5})$$

where P_{trans} is the transit probability and P_{det} is the detection efficiency. The probability of eclipse is 1% for an Earth-sized planets in the habitable zone of a white dwarf, and Belardi et al. (2016) calculated a detection efficiency of 68% given our observing window. Therefore our effective sample size $N' = 0.0068N = 5.45$, and we constrain the frequency of Earth-sized planets orbiting in the habitable zone of a white dwarf to $< 37\%$ at the 95% confidence level. Our results are slightly higher than the constraints on habitable zone Earth-sized planets around white dwarfs of $< 28\%$ found by Van Sluijs & Van Eylen (2018) due to our slightly smaller sample size. If we include the 309 WDs from Van Sluijs & Van Eylen (2018) with short cadence K2 observations, which should have similar detection rates to our sample, we find a maximum occurrence rate of $\leq$30%. However, the DECam survey has high cadence observations for our entire WD sample, giving us a better overall detection probability for orbital periods consistent with habitable zone planets around white dwarfs (4-32 hrs).

3.4 Variability

3.4.1 Variable Candidate Selection

We follow the same procedure outlined in Dame et al. (2019) to find variable sources. We use the VARTOOLS suite of software (Hartman & Bakos, 2016) to run a Lomb-Scargle periodogram analysis on all the sources in our field. From this, we get the five most significant peaks in the periodogram and their corresponding false alarm probability (FAP). Figure 3.4 shows the distribution of FAP values as a function of period. We select all sources with $log_{10}(\text{FAP}) \leq -6.2$, the theoretical 5σ confidence level, with more negative values having a higher probability of real variability.

We find 1940 variable candidates with at least one period with $log_{10}(\text{FAP}) \leq -6.2$. However, systematic effects such as red noise can introduce a larger spread in $log_{10}(\text{FAP})$ values at longer periods, and we expect the real 5σ confidence level to be more negative than the theoretical limit. Therefore, we inspect each candidate with the Period04 package (Lenz & Breger, 2014). We compare the amplitudes of the observed peaks with the median amplitude, $\langle \text{A} \rangle$, of the Fourier Transform and look for significant peaks ($\geq 5\langle \text{A} \rangle$).

As in the first field, the majority of our initial candidates either do not show a significant peak after analysis with Period04, exhibit obvious problems due to attempts to fit outliers and minor zero-point magnitude differences across nights due to our calibration method, or show false positives occurring around 6, 8, 12, and 24 hours due to our observing window from the ground. Of our 1940 initial candidates, we find 83 objects that show evidence of genuine variability in their light curves. Table 3.1 presents the coordinates, periods, CFHT Legacy Survey *ugriz* photometry, and variable types for these sources.

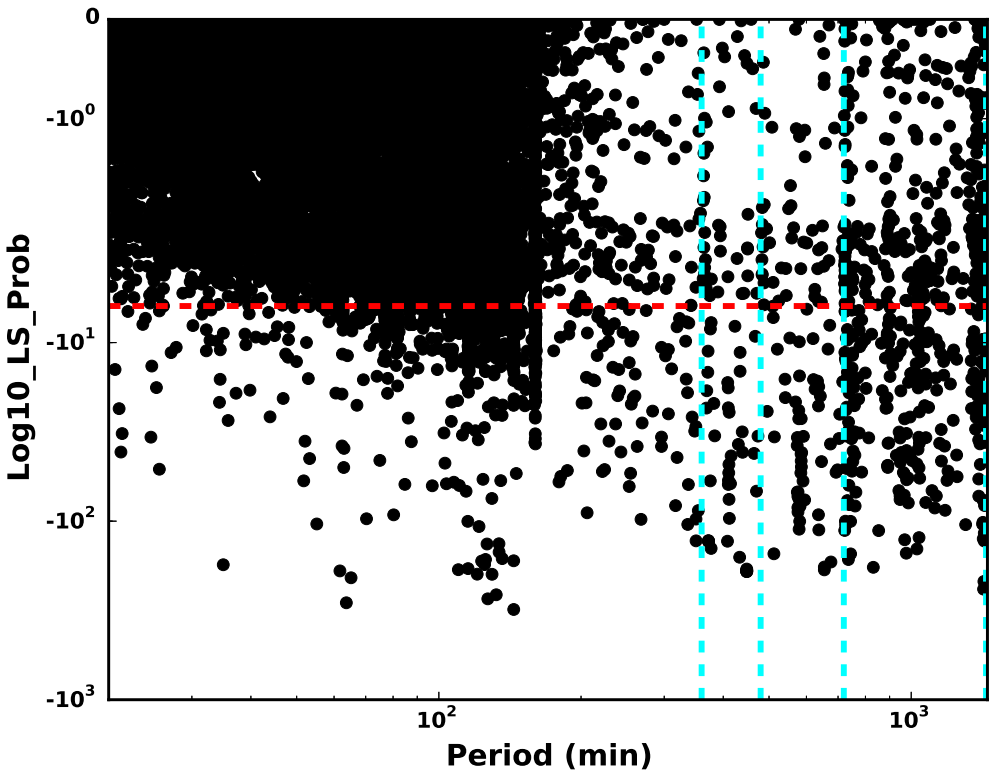

Fig. 3.4.— The false alarm probability ($log_{10}(FAP)$) as a function of period for our sample. The red dashed line shows the theoretical 5σ confidence level; we select all objects below this line as our initial variable candidates. Cyan dotted lines mark periods of 6, 8, 12, and 24 hrs.

We use the colours, periods, and general shape of the light curves to determine type of variable star. Figure 3.5 shows the color-color diagram for our variable targets. For reference, we also plot all non-variable objects with g<20 in the field, and the predicted colors[a] for pure hydrogen white dwarfs with $\log g$= 7, 8, and 9 (Holberg & Bergeron, 2006; Kowalski & Saumon, 2006; Tremblay et al., 2011; Bergeron et al., 2011). Additionally, 81 of our variable targets are detected in *Gaia*. Of these, only 22 have parallax over error measurements ≥ 4. Therefore, we instead use the geometric distance estimates from Bailer-Jones et al. (2018), inferred from Bayesian analysis with a weak distance prior based on an exponentially decreasing space density such that the probability *P(r|L)*

$$P(r|L) = \begin{cases} \frac{1}{2L^3} r^2 e^{-r/L}, & \text{if } r > 0 \\ 0, & \text{otherwise} \end{cases} \tag{3.6}$$

where r is the distance and $L > 0$ is a scale length. We plot the color-magnitude diagram for these 85 variable targets in Figure 3.6. We also include non-variable sources (grey points) detected with *Gaia* with parallax over error $\geq$ 4 and the model sequence (cyan line) for a H atmosphere white dwarf of $\log g = 7$ (top) and $\log g = 8$ (bottom).

We recover 26 variable sources previously identified in the Catalina survey. Our classifications and periods are in good agreement with those of the Catalina survey with the exception of J0859−0224 (discussed below). We find 53 binary systems, 13 δ Scuti pulsators, 10 RR Lyrae, 5 ZZ Ceti pulsators, and two sources of unknown variable type.

[a]http://www.astro.umontreal.ca/ bergeron/CoolingModels/

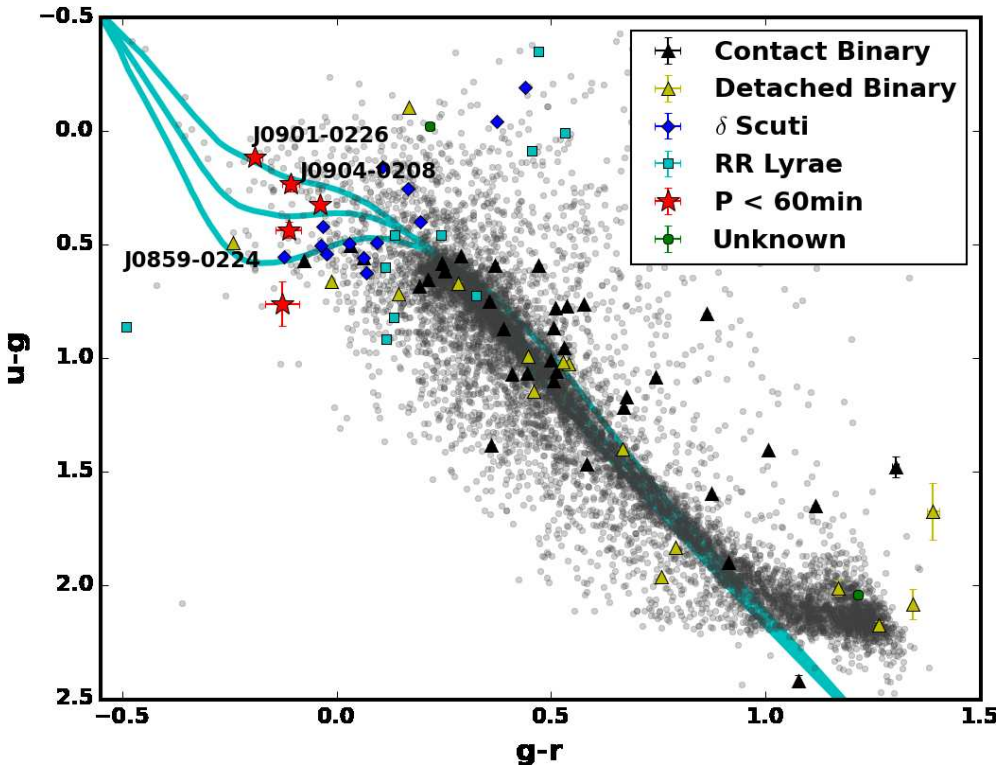

Fig. 3.5.— Colour-colour diagrams for our 87 variable objects and non-variable objects with g<20 mag (grey points). Colors are taken from the CFHT Legacy Survey *ugriz* photometry (AB scale). Predicted colors for a $\log g = 9.0$, 8.0, and 7.0 (top to bottom) white dwarf with pure hydrogen atmospheres (cyan lines) are shown for reference.

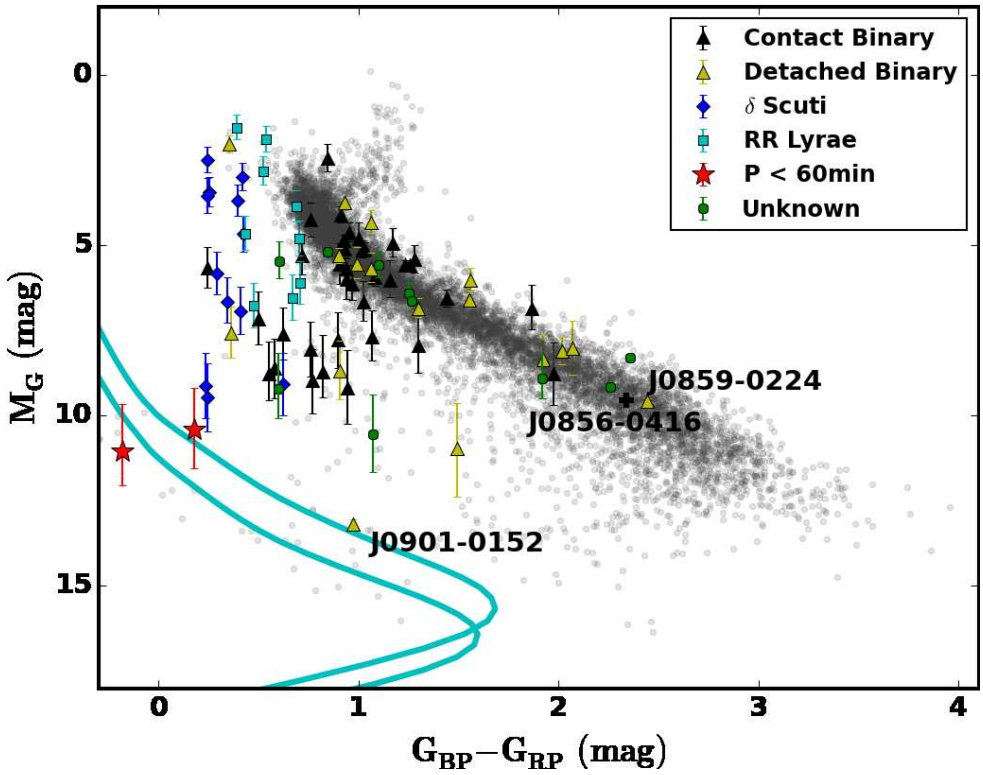

Fig. 3.6.— Colour-magnitude diagram for our 85 variable objects detected with *Gaia*. Symbols are the same as Figure 3.5. Non-variable sources from our survey with parallax over error ≥ 4 are shown as grey points. The transit candidate J0856−0416 is shown as a black cross. Cyan lines show the model sequence for an H atmosphere white dwarf with $\log g = 7$ (top) and $\log g = 8$ (bottom).

3.4.2 J0859−0224

Figure 3.7 shows the phase-folded light curve for J0859−0224 from the Catalina survey (top) and this work (bottom), along with the periods calculated for each. Drake et al. (2014) classified J0859−0224 as a contact binary. However, our minute-cadence data shows clear transits that were not observed in the Catalina survey. The short duration (≈30 min) and sharp ingress and egress of these transits are consistent with a white dwarf + M dwarf binary, and the observed sinusoidal variations are consistent with ellipsoidal modulation. The light curve is essentially identical to other eclipsing white dwarf + M dwarf binaries showing ellipsoidal variation found in Parsons et al. (2017). The binary nature of J0859−0224 is clearly visible by comparing its position in Figures 3.5 and 3.6. Colours for J0859−0224 based on broad *Gaia* filters are consistent with a roughly M3 spectral type M-dwarf (Gagné & Faherty, 2018), as is its position in Figure 3.6. However, colours based on Megacam *ugr* filters (Figure 3.5) place J0859−0224 near our newly identified ZZ Ceti white dwarfs, and suggest a hot white dwarf.

J0859−0224 is the second eclipsing white dwarf + M dwarf binary detected in the DECam survey. About 22% of field white dwarfs have late-type stellar companions (Farihi et al., 2005), with 3.4% of these systems showing eclipses with $P < 2$ day orbits (Parsons et al., 2013). Hence, the frequency of eclipsing white dwarf + M dwarf binaries is likely around 0.75% for randomly oriented orbits. The Besançon Galaxy model predicts ≈ 800 white dwarfs in the entire survey, and we would expect to find up to 6 eclipsing white dwarf + M dwarfs in our dataset. Hence, the discovery of a second such system in our survey is not surprising.

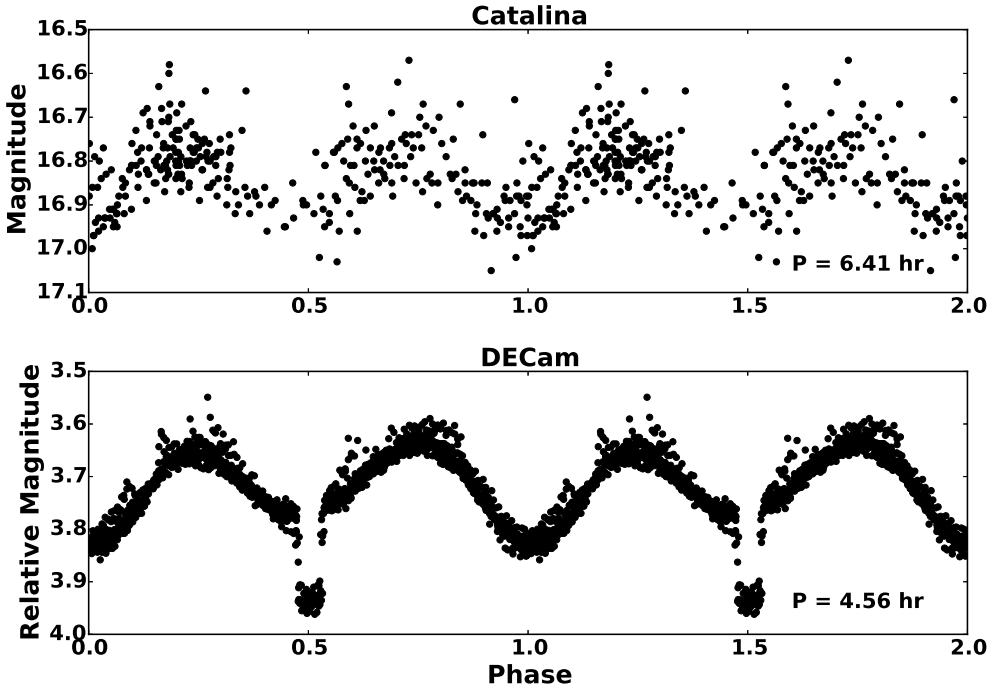

Fig. 3.7.— Phase-folded light curve of J0859−0224 from the Catalina survey (top, Drake et al., 2014) and this work(bottom). We observe a previously unseen transit consistent with a detached WD+dM binary.

Table 3.1. Variable objects from the second and third fields.

Object	RA	Dec	Period (hr)	u	g	r	i	z	Type	
J0850−0456	08:50:48.837	−04:56:41.74	4.56	...	20.07	19.37	19.00	18.81	contact	1
J0851−0418	08:51:02.348	−04:18:43.84	6.49	19.53	17.94	17.06	16.85	16.73	contact	2
J0851−0452	08:51:31.078	−04:52:01.03	6.82	17.70	17.11	16.64	16.54	16.56	contact	2
J0851−0420	08:51:49.127	−04:20:22.93	6.99	18.02	17.07	16.54	16.40	15.80	contact	2
J0851−0417	08:51:53.281	−04:17:27.68	6.56	20.30	19.72	19.53	19.43	19.52	contact	1
J0851−0350	08:51:59.635	−03:50:51.63	...	19.23	17.83	17.16	16.99	16.63	detached	1
J0852−0513	08:52:33.325	−05:13:43.89	6.86	17.80	16.70	16.20	16.20	15.90	contact	1
J0852−0341	08:52:49.720	−03:41:55.42	6.32	17.69	16.92	16.35	16.32	16.13	contact	1
J0853−0404	08:53:02.309	−04:04:02.03	6.97	20.55	19.68	19.29	19.16	19.13	contact	1
J0853−0343	08:53:10.715	−03:43:31.75	...	19.41	17.44	16.69	16.39	16.03	detached	1
J0854−0521	08:54:24.303	−05:21:37.52	7.29	19.39	18.58	17.72	17.66	17.86	contact	2
J0854−0409	08:54:33.564	−04:09:34.48	8.36	18.66	18.09	18.17	18.25	18.41	contact	1
J0854−0526	08:54:55.706	−05:26:51.83	...	15.35	15.46	15.29	15.58	15.07	detached	2
J0855−0340	08:55:43.451	−03:40:21.81	7.00	17.90	17.03	16.53	16.48	16.35	contact	2
J0856−0444	08:56:09.760	−04:44:13.56	3.03	18.22	17.15	16.74	16.58	16.12	contact	2
J0856−0510	08:56:26.280	−05:10:23.14	6.11	20.94	20.46	19.71	19.42	19.49	contact	1
J0856−0453	08:56:26.961	−04:53:38.75	5.32	...	17.84	17.31	17.18	17.28	contact	1
J0856−0430	08:56:42.935	−04:30:52.44	...	23.08	20.99	19.65	18.73	18.48	detached	1
J0856−0442	08:56:43.074	−04:42:32.13	8.33	20.73	19.98	19.63	19.74	19.74	contact	1
J0856−0458	08:56:55.038	−04:58:15.35	9.07	20.02	19.35	19.37	19.58	19.43	detached	1
J0857−0412	08:57:12.499	−04:12:54.80	22.43	18.93	17.92	17.39	17.15	17.06	detached	1
J0857−0456	08:57:41.354	−04:56:36.41	6.75	18.81	17.34	16.76	16.61	16.33	contact	1
J0859−0224	08:59:42.165	−02:24:04.56	4.58	20.01	18.52	17.48	16.42	15.88	contact	2
J0859−0208	08:59:46.959	−02:08:12.42	10.74	22.65	...	20.88	20.65	20.63	detached	1
J0900−0200	09:00:08.317	−02:00:40.77	...	18.92	17.77	17.31	17.28	17.05	detached	1

Table 3.1—Continued

Object	RA	Dec	Period (hr)	u	g	r	i	z	Type	
J0900−0301	09:00:17.068	−03:01:05.87	7.70	20.12	19.47	19.26	19.21	19.21	contact	1
J0900−0205	09:00:21.198	−02:05:31.89	5.95	21.97	19.55	18.47	17.74	17.35	contact	2
J0900−0304	09:00:54.891	−03:04:25.17	6.72	22.68	21.20	19.90	19.05	18.61	contact	1
J0900−0217	09:00:58.444	−02:17:40.11	60.38	16.16	15.66	15.91	15.61	14.97	detached	2
J0901−0218	09:01:02.499	−02:18:39.11	...	22.24	20.23	19.06	18.35	17.98	detached	1
J0901−0230	09:01:30.700	−02:30:38.80	6.85	18.30	16.91	16.56	16.41	15.70	contact	2
J0901−0152	09:01:38.924	−01:52:29.18	5.91	19.55	18.53	17.99	17.85	17.84	detached	1
J0902−0316	09:02:09.334	−03:16:48.27	5.40	18.67	17.61	17.16	17.25	17.00	contact	2
J0902−0218	09:02:12.928	−02:18:22.01	8.00	16.90	16.40	16.36	16.21	15.62	contact	1
J0902−0125	09:02:14.757	−01:25:51.54	6.30	23.81	22.14	20.75	20.18	19.96	detached	1
J0902−0232	09:02:28.513	−02:32:13.31	...	21.48	19.31	18.06	17.46	17.03	detached	1
J0902−0311	09:02:54.817	−03:11:17.66	6.20	20.30	19.29	18.79	18.55	18.48	contact	1
J0903−0234	09:03:04.265	−02:34:37.57	...	17.49	16.77	16.63	16.48	15.97	detached	1
J0903−0145	09:03:09.619	−01:45:05.67	6.50	17.60	16.42	15.75	15.41	15.10	contact	2
J0903−0235	09:03:44.930	−02:35:46.09	6.38	19.16	18.39	17.87	17.66	17.52	contact	2
J0903−0131	09:03:56.067	−01:31:09.89	7.71	19.62	17.72	16.80	17.09	16.24	contact	2
J0904−0207	09:04:06.977	−02:07:09.41	...	20.57	19.90	19.62	19.48	19.59	detached	1
J0904−0149	09:04:13.348	−01:49:14.60	6.33	19.52	18.46	17.94	17.86	17.88	contact	2
J0904−0310	09:04:15.096	−03:10:13.54	7.87	19.96	19.41	19.12	19.01	19.27	contact	1
J0904−0309	09:04:19.827	−03:09:38.69	6.20	17.22	16.60	16.35	16.23	15.90	contact	2
J0904−0221	09:04:29.695	−02:21:15.11	8.04	19.12	18.04	17.29	17.03	16.90	contact	2
J0904−0304	09:04:30.645	−03:04:36.76	7.23	18.36	17.68	17.49	17.30	17.40	contact	1
J0904−0207	09:04:35.820	−02:07:42.86	5.95	19.59	18.37	17.70	17.39	17.39	contact	1
J0904−0139	09:04:40.914	−01:39:58.20	5.13	20.85	20.26	19.89	19.79	19.96	contact	1
J0905−0148	09:05:05.429	−01:48:11.25	17.71	17.78	16.79	16.34	16.37	15.95	detached	2

Table 3.1—Continued

Object	RA	Dec	Period (hr)	u	g	r	i	z	Type	
J0905−0139	09:05:09.498	−01:39:12.73	31.62	19.55	17.72	16.93	16.69	16.17	detached	1
J0906−0236	09:06:07.458	−02:36:20.97	6.24	20.52	19.93	19.69	19.74	19.72	contact	1
J0906−0211	09:06:44.387	−02:11:02.21	3.85	19.19	18.41	17.88	17.68	17.71	contact	1
Object	RA	Dec	Period (hr)	u	g	r	i	z	Type	Source
J0852−0432	08:52:57.502	−04:32:30.93	14.81	18.94	18.02	17.91	17.61	17.92	RR Lyrae	1
J0852−0447	08:52:40.152	−04:47:27.31	8.11	16.54	16.08	15.83	16.21	15.95	RR Lyrae	2
J0853−0521	08:53:09.908	−05:21:54.07	13.19	17.81	16.95	17.44	17.30	17.44	RR Lyrae	3
J0853−0417	08:53:24.993	−04:17:02.97	12.83	16.87	16.40	16.26	16.29	16.37	RR Lyrae	3
J0856−0420	08:56:58.438	−04:20:55.34	30.77	16.50	16.41	15.95	16.13	15.70	RR Lyrae	3
J0857−0416	08:57:01.616	−04:16:59.19	13.26	19.11	19.45	18.98	19.01	19.09	RR Lyrae	3
J0900−0246	09:00:57.215	−02:46:29.00	8.12	18.30	17.70	17.59	17.62	17.45	RR Lyrae	2
J0902−0209	09:02:01.182	−02:09:26.07	15.48	19.40	18.58	18.45	18.42	18.44	RR Lyrae	1
J0902−0233	09:02:03.204	−02:33:44.91	15.19	19.22	18.50	18.17	18.09	18.02	RR Lyrae	1
J0903−0311	09:03:21.184	−03:11:50.91	14.04	18.16	18.15	17.61	17.79	17.72	RR Lyrae	3
Object	RA	Dec	Period (min)	u	g	r	i	z	Type	Source
J0851−0513	08:51:36.735	−05:13:17.87	66.83	16.72	16.57	16.46	16.64	16.48	δ Scuti	1
J0851−0458	08:51:39.170	−04:58:16.20	63.52	17.51	17.11	16.92	17.06	17.02	δ Scuti	1
J0851−0359	08:51:41.569	−03:59:29.77	55.66	20.67	20.11	20.23	20.26	20.81	δ Scuti	1
J0854−0521	08:54:36.998	−05:21:48.78	51.78	19.40	18.84	18.78	18.78	18.89	δ Scuti	1
J0854−0456	08:54:46.803	−04:56:26.43	65.16	18.52	18.11	18.14	18.08	18.23	δ Scuti	1
J0855−0447	08:55:58.858	−04:47:56.11	79.02	16.31	16.06	15.89	15.96	15.89	δ Scuti	1
J0856−0402	08:56:33.950	−04:02:39.97	63.44	19.34	18.84	18.81	18.82	18.93	δ Scuti	1
J0856−0436	08:56:55.662	−04:36:20.75	64.52	18.71	18.20	18.24	18.27	18.38	δ Scuti	1

Table 3.1—Continued

Object	RA	Dec	Period (hr)	u	g	r	i	z	Type	
J0859−0148	08:59:58.902	−01:48:36.65	60.26	16.54	16.73	16.29	16.33	16.29	δ Scuti	1
J0900−0147	09:00:48.355	−01:47:37.52	63.69	16.97	17.01	16.64	16.69	16.75	δ Scuti	1
J0904−0304	09:04:52.996	−03:04:05.72	55.15	20.75	20.26	20.17	20.23	20.32	δ Scuti	1
J0906−0221	09:06:00.944	−02:21:28.54	62.36	20.70	20.16	20.19	20.25	20.33	δ Scuti	1
J0906−0250	09:06:21.864	−02:50:08.85	62.91	18.33	17.71	17.64	17.66	17.79	δ Scuti	1
Object	RA	Dec	Period (min)	u	g	r	i	z	Type	Source
J0900−0241	09:00:16.012	−02:41:50.32	18.96	20.75	20.42	20.46	20.59	20.83	ZZ Ceti	1
J0901−0227	09:01:25.780	−02:27:59.75	22.38	20.96	20.20	20.33	24.36	20.87	ZZ Ceti	1
			27.79	...	20.17	20.29	20.47	20.51		
J0901−0226	09:01:43.447	−02:26:04.84	6.67	22.19	21.95	22.06	22.28	22.39	ZZ Ceti	1
J0904−0208	09:04:44.317	−02:08:19.04	6.07	21.33	21.21	21.40	21.57	21.75	ZZ Ceti	1
J0905−0202	09:05:20.985	−02:02:18.02	13.00	22.51	22.07	22.19	22.32	22.49	ZZ Ceti	1
			16.32							
Object	RA	Dec	Period (min)	u	g	r	i	z	Type	Source
J0901−0311	09:01:35.368	−03:11:43.14		21.77	19.72	18.51	17.74	17.44	...	1
J0902−0142	09:02:46.548	−01:42:01.84		20.91	20.93	20.71	20.36	20.45	...	1

Note. — Coordinates, periods, *ugriz* photometry from the CFHT Legacy Survey, and determined variable type for out 83 variable candidates. Sources are (1) this work, (2) Drake et al. (2014), (3) Drake et al. (2013). CFHT Legacy Survey photometry is not available for J0850−0456, J0856−0453, and J0901−0227. For these sources, we instead report *griz* photometry from Pan-STARRS. J0901−0227 is also detected in SDSS, and we include SDSS *ugriz* photometry in addition to Pan-STARRS photometry.

3.4.3 J0901−0152

Based on its position in Figure 2.5, J0901−0152 appears to be an extremely low mass (ELM) white dwarf ($5 < \log g < 7$). The progenitors of ELM WDs have main sequence lifetimes older than the age of the universe, meaning that these stars must form in binary systems. The phase-folded light curve for J0901−0152 is shown in Figure 3.8, and we classify it as a detached binary with P = 5.91 hrs. This period is consistent with the median period of 5.4 hrs found for ELM WD binaries found by Brown et al. (2016). Interestingly, the observed ellipsoidal variation appears too large to be caused by an ELM companion given the determined orbital period. However, radial velocity measurements of the system are needed to constrain the nature of the companion.

3.4.4 ZZ Ceti

We find 5 ZZ Ceti candidates with periods ranging from 6.07-22.38 minutes. Figure 2.4 shows that these candidates are consistent with predicted colours for H atmosphere white dwarfs. Only two of our ZZ Ceti candidates are bright enough to be detected in *Gaia*, and Figure 2.5 shows that *Gaia* measurements are also consistent with H atmosphere white dwarf models. With the exception of the white dwarf companion of PSR 1738+0333, the five ZZ Ceti identified in this work, along with the two identified in the first field (Dame et al., 2019), are the faintest currently known ZZ Ceti white dwarfs.

J0904−0208 and J0901−0226 both appear to be massive WDs. They lie near the $\log g = 9$ track in Figure 2.4, and their ≈ 6 min periods are consistent with the periods of known massive ZZ Ceti white dwarfs. As white dwarfs cool, their interiors undergo crystallization, releasing latent heat that can lengthen cooling times by several Gyrs. Pulsating white dwarfs can probe this crystallization pro-

cess, but only massive white dwarfs have sufficiently crystallized cores while they are in the ZZ Ceti instability strip. The only currently known ultramassive ZZ Ceti are BPM 37093 (Kanaan et al., 1992, 2005), GD 518 (Hermes et al., 2013), and SDSS J0840+5222 (Curd et al., 2017).

Including results from the first field, we find 7 ZZ Ceti pulsators in our survey, or 0.87% of the expected white dwarfs. The Besançon Galaxy model predicts 20 H atmosphere white dwarfs consistent with the instability strip with magnitudes brighter than our completeness limit of g = 22.5. The faintest ZZ Ceti we observe is J0905−0202 with $g = 22.51$. Therefore, the Besançon Galaxy model gives a theoretical ZZ Ceti fraction of 1.9%, in reasonably good agreement with our observed fraction.

3.5 Conclusions

We present results from the final two fields of the DECam minute-cadence survey. We construct and analyze the light curves of the 58487 point sources in the fields for evidence of planetary transits around a white dwarf. While we find a curious pair of ∼minute duration dips around the likely M dwarf J0856−0416, we find no compelling evidence consistent with planetary eclipses of a white dwarf. Combining our results with the results from our first field, we constrain the occurrence rate of Earth-sized planets within the habitable zone of a white dwarf to $< 37\%$ at the 95% confidence level. Additionally, we identify 57 new variable objects: 34 binary systems, 13 δ Scuti type pulsators, 3 RR Lyrae, and 5 ZZ Ceti white dwarfs, two of which are potentially massive enough to have begun crystallization in their cores. We also identify a new eclipsing white dwarf + M dwarf binary showing ellipsoidal variation previously misidentified in the Catalina survey.

As the next generation of large-scale, high cadence surveys, such as Super-

WASP, the Next-Generation Transit Survey, the Transiting Exoplanet Survey Satellite, and ZTF, begin to release data, the possibility of observing previously unobserved or unknown phenomena increases. LSST is expected to observe 10^7 white dwarfs with $r < 24.5$ mag over a ten year baseline. Cortés & Kipping (2019) showed that although the temporal coverage of LSST is poor, the phase coverage is sufficient to search for even Ceres-sized objects around white dwarfs. They estimate that an occurrence rate of just 10% for habitable earth-sized planets orbiting white dwarfs should still yield ∼100 detections. The next few decades should provide stringent constraints on the rarity of such systems, and, hopefully, reveal the first planetary system around a white dwarf.

Acknowledgements

This work is in part supported by NASA under grant NNX14AF65G. Based on observations at Cerro Tololo Inter-American Observatory, National Optical Astronomy Observatory (NOAO Prop. ID:2014B-0064 and PI: M. Kilic and NOAO Prop. ID:2015A-0107 and PI: C. Belardi), which is operated by the Association of Universities for Research in Astronomy (AURA) under a cooperative agreement with the National Science Foundation.

This project used data obtained with the Dark Energy Camera (DECam), which was constructed by the Dark Energy Survey (DES) collaboration. Funding for the DES Projects has been provided by the DOE and NSF (USA), MISE (Spain), STFC (UK), HEFCE (UK). NCSA (UIUC), KICP (U. Chicago), CCAPP (Ohio State), MIFPA (Texas A&M), CNPQ, FAPERJ, FINEP (Brazil), MINECO (Spain), DFG (Germany) and the collaborating institutions in the Dark Energy Survey, which are Argonne Lab, UC Santa Cruz, University of Cambridge, CIEMAT-Madrid, University of Chicago, University College London, DES-Brazil

Consortium, University of Edinburgh, ETH Zurich, Fermilab, University of Illinois, ICE (IEEC-CSIC), IFAE Barcelona, Lawrence Berkeley Lab, LMU Munchen and the associated Excellence Cluster Universe, University of Michigan, NOAO, University of Nottingham, Ohio State University, University of Pennsylvania, University of Portsmouth, SLAC National Lab, Stanford University, University of Sussex, and Texas A&M University.

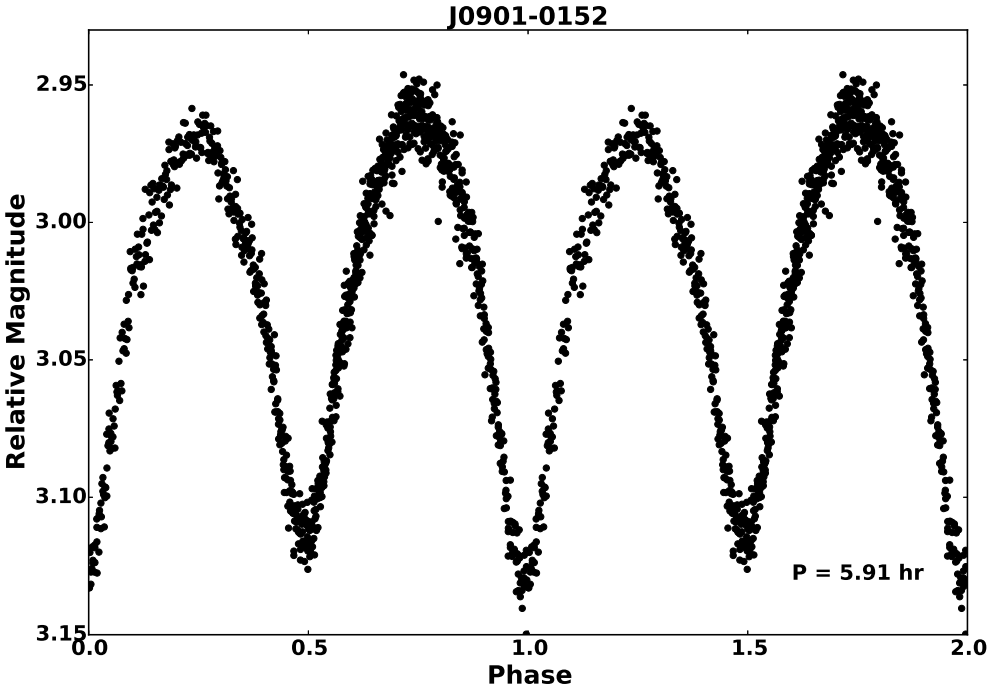

Fig. 3.8.— Phase-folded light curve of J0901−0152.

Chapter 4

Conclusions

The Kepler/K2 mission and other planetary searches have shown that exoplanets are common around main sequence stars. However, what happens to these planets as their host stars evolve is still unknown. Theoretical models predict that planets within a few AU of their host star should be engulfed and destroyed as the star evolves, but post-main-sequence evolution is complicated, and even the fate of our own solar system is uncertain (Veras, 2016; Villaver & Livio, 2007). Debris disks and metal pollution in the atmospheres of white dwarfs suggest that something must survive beyond a star's post-main-sequence evolution. Recent observations of a disintegrating planetesimal around WD 1145+017 and a possible leftover planetary core around the white dwarf SDSS J1228+1040 get tantalizingly close, but we have yet to detect a solid body planetary companion orbiting a white dwarf.

The DECam minute cadence survey was the first survey designed specifically to search for such planets. Previous surveys suffered either from a lack of white dwarfs or cadences too low to observe these minute timescale events. The Dark Energy Camera's wide field of view allows simultaneous observations of hundreds of white dwarfs with a single pointing. We obtain ∼90 second cadence g-band images over eight half-nights for three separate pointings, covering 9 deg^2 of the night sky with S/N $\geq$ 5 for sources brighter than $g = 24.5$ AB mag.

4.1 The First Field

In Chapter 2, we presented the results from the first DECam field. Previous work by Belardi et al. (2016) focused on easily identified high proper motion white

dwarfs, but missed hundreds more low proper motion white dwarfs predicted by galaxy models. In order to search for planets around these missing white dwarfs, we extended the analysis to include all of the 31732 point sources detected in the field. We searched for 5σ dips in the light curves of our sources. These initial transit candidates were manually inspected to remove sources near the edge of the CCD, near bad pixels or saturated stars, or that appeared elongated in the images. In order to remove statistical false positives, we generated difference images for all transit candidates passing visual inspection using HOTPANTS. Of our 5244 initial transit candidates, only 8 passed visual inspection. None of these transit candidates showed a matching residual in the difference image, and so are not real. We found no evidence of a planetary transit of a white dwarf in the first field.

Additionally, we analyzed the point sources in the field for other sources of stellar variability. We used the VARTOOLS package to select initial variability candidates with a false alarm probability below the theoretical 5σ limit. However, the theoretical limit does not take into account systematic effects such as red noise. Therefore, we inspected our initial variable candidates with the Period04 package. Of our initial 889 candidates, 213 did not show a significant peak in Period04. Additionally, many of the remaining candidates showed false peaks due either to our observing window or attempts to overfit the data. We found 49 objects that showed genuine periodic variability in their light curves. Nine of these objects were previously discovered systems from the Catalina survey. We determined the type of variable star using colors from the CHFTLS photometry, periods, and the general shape of the light curves. Our results included 23 detached or contact stellar binaries, 1 eclipsing white dwarf + M dwarf binary, 16 δ Scuti, three RR Lyrae, two ZZ Ceti pulsators, and four objects of undetermined type.

4.2 The Second and Third Fields

In Chapter 3, we presented the results from the second and third DECam fields, containing 58487 point sources. Following the same procedures from Chapter 2, we found one object, J0856−0416, that showed two genuine, significant dips lasting ∼1 minute, proving that our process is capable of detecting such brief events. However, *Gaia* observations show that this object is not a white dwarf, but instead most likely an M-dwarf. The cause of minute timescale dips around a main sequence star is uncertain, and further observations are needed to understand these events.

We found no evidence of planetary companions around a white dwarf. Based on an estimated 802 white dwarfs in the survey, we calculated the maximum occurrence rate for habitable earth-sized planets around white dwarfs to be ≤37% at the 95% confidence level. Our results are slightly higher than estimates from Van Sluijs & Van Eylen (2018) due to our slightly smaller sample size. However, with high cadence observations for the entire WD sample, the DECam survey has a better overall detection probability for planets with orbital periods of 4-32 hrs. If we include the 309 WDs from Van Sluijs & Van Eylen (2018) with short cadence K2 observations, we find a maximum occurrence rate of ≤30%, in good agreement with previous estimates. With an occurrence rate for habitable earth-sized planets around main sequence stars of ∼ 22% (Petigura et al., 2013), our constraints indicate that such planets are not significantly more common around white dwarfs that main sequence stars. Our null detection is also in agreement with theoretical predictions from Villaver & Livio (2007) that all but the most massive planets within 1.5-5 AU (for main sequences masses of 1-5 $M_{\odot}$) should be destroyed during the post-main-sequence evolution of their host star.

We found an additional 83 variable objects in these fields. We found 53 binary

systems, 13 δ Scuti pulsators, 10 RR Lyrae, five ZZ Ceti pulsators, and two sources of unknown variable type. Of these, we recovered 26 objects previously discovered in the Catalina survey. One of these sources, J0859−0224, was originally classified as a contact binary. However, our observations showed previously undetected 17.8 min eclipses, marking this system as a detached, eclipsing white dwarf + M dwarf binary undergoing ellipsoidal variation. J0859−0224 also highlights the importance of high cadence surveys, showing that long cadence observations can hide critical features and make interesting systems appear ordinary. We found one likely extremely low mass white dwarf, based on *Gaia* observations, though follow-up observations are necessary to confirm and determine the nature of the companion. We also found five ZZ Ceti, two of which appear massive enough to have begun crystallization in their cores, though spectroscopic follow-up will be necessary to confirm. With only three currently known ultramassive ZZ Ceti, these respresent a potentially significant increase. All seven ZZ Ceti detected in our survey have $g > 20$ mag. With the exception of the white dwarf companion of PSR 1738+0333, these new ZZ Ceti pulsators are the faintest currently known by at least a magnitude.

4.3 Future Work

The DECam minute cadence survey observed over 90,000 targets for eight half-nights, and the work presented in this dissertation only scratches the surface of this fantastic data set. Though we found 132 periodic variable systems with periods up to a few days, our process was not sensitive to non-periodic sources of variability such as flares, or suited to detect asteriods. Though an analysis of these objects is beyond the scope of this work, the DECam minute cadence survey offers a wealth of high cadence observations of such objects. Additionally, our high

cadence observations detected unexpected and unexplained minute-duration dips around a likely M-dwarf star. With observations of over 90,000 stars, there may other new, previously unseen phenomena waiting to be found.

Although we did not find evidence of any planetary companions around a white dwarf, such systems, if they exist, cannot remain hidden for long. Advances in technology are continuously driving new generations of large-scale surveys to fainter magnitudes and higher cadences. The processes described in this work are directly applicable to upcoming large-scale surveys, such as TESS, ZTF, SuperWASP, and the Next-Generation Transit Survey. In particular, LSST is predicted to observe $\sim 10^7$ white dwarfs with $r < 24.5$ mag over a ten year baseline. Cortés & Kipping (2019) have shown that despite poor temporal coverage, LSST will be capable of detecting even Ceres-sized companions around white dwarfs for orbital periods less than 10 days. Simulated dectection rates range from $5\text{x}10^{-6}$ to $4\text{x}10^{-4}$. With such a large sample of white dwarfs, LSST should detect planetary companions for occurrence rates greater than $\sim 10^{-4}$, three orders of magnitude lower than current constraints. With LSST scheduled to begin observations in 2022, unless such systems are exceedingly rare, we should see the first planets around white dwarfs within the next 15 years.

References

Agol, E., 2011, ApJ, 731, L31

Alibert, Y., Mordasini, C., & Benz, W. 2011, A&A, 526, A63

Amaro-Seoane, P., Aoudia, S., Babak, S., et al. 2013, GW Notes, Vol. 6, p. 4-110, 6, 4

Bailer-Jones, C. A. L., Rybizki, J., Fouesneau, M., Mantelet, G., & Andrae, R. 2018, AJ, 156, 58

Bakos, G., Noyes, R. W., Kovács, G., et al. 2004, PASP, 116, 266

Barber, S. D., Belardi, C., Kilic, M., & Gianninas, A. 2016, MNRAS, 459, 1415

Becker, A. 2015, Astrophysics Source Code Library, ascl:1504.004

Belardi, C., Kilic, M., Munn, J. A., et al. 2016, MNRAS, 462, 2506

Bellm, E., & Kulkarni, S. 2017, Nature Astronomy, 1, 0071

Bergeron, P., Leggett, S. K., & Ruiz, M. T. 2001, ApJS, 133, 413

Bergeron, P., Wesemael, F., Dufour, P., et al. 2011, ApJ, 737, 28

Bertin, E., Mellier, Y., Radovich, M., et al. 2002, Astronomical Data Analysis Software and Systems XI, 281, 228

Bramich, D. M., Vidrih, S., Wyrzykowski, L., et al. 2008, MNRAS, 386, 887

Brown, W. R., Gianninas, A., Kilic, M., Kenyon, S. J., & Allende Prieto, C. 2016, ApJ, 818, 155

Brown, W. R., Kilic, M., & Gianninas, A. 2017, ApJ, 839, 23

Chang, S.-W., Protopapas, P., Kim, D.-W., & Byun, Y.-I. 2013, AJ, 145, 132

Cortés, J., & Kipping, D. 2019, MNRAS,

Cuillandre, J.-C. J., Withington, K., Hudelot, P., et al. 2012, Proceedings of the SPIE, 8448, 84480M

Curd, B., Gianninas, A., Bell, K. J., et al. 2017, MNRAS, 468, 239

Dame, K., Gianninas, A., Kilic, M., et al. 2016, MNRAS, 463, 2453

Dame, K., Belardi, C., Kilic, M., et al. 2019, MNRAS,

Drake, A. J., Catelan, M., Djorgovski, S. G., et al. 2013, ApJ, 763, 32

Drake, A. J., Graham, M. J., Djorgovski, S. G., et al. 2014, ApJS, 213, 9

Faedi, F., West, R. G., Burleigh, M. R., Goad, M. R., & Hebb, L. 2011, MNRAS, 410, 899

Farihi, J., Becklin, E. E., & Zuckerman, B. 2005, ApJS, 161, 394

Fontaine, G., & Brassard, P. 2008, PASP, 120, 1043

Fulton, B. J., Tonry, J. L., Flewelling, H., et al. 2014, ApJ, 796, 114

Gaia Collaboration, Babusiaux, C., van Leeuwen, F., et al. 2018, A&A, 616, A10

Gagné, J., & Faherty, J. K. 2018, ApJ, 862, 138

Gänsicke, B. T., Aungwerojwit, A., Marsh, T. R., et al. 2016, ApJ, 818, L7

Garg, A., Stubbs, C. W., Challis, P., et al. 2007, AJ, 133, 403

Gentile Fusillo, N. P., Tremblay, P.-E., Gänsicke, B. T., et al. 2019, MNRAS, 482, 4570

Giammichele, N., Charpinet, S., Brassard, P., & Fontaine, G. 2017, A&A, 598, A109

Gianninas, A., Bergeron, P., & Ruiz, M. T. 2011, ApJ, 743, 138

Hartman, J. D., & Bakos, G. Á. 2016, Astronomy and Computing, 17, 1

Hermes, J. J., Kepler, S. O., Castanheira, B. G., et al. 2013, ApJ, 771, L2

Holberg, J. B., & Bergeron, P. 2006, AJ, 132, 1221

Holberg, J. B., Oswalt, T. D., Sion, E. M., & McCook, G. P. 2016, MNRAS, 462, 2295

Iben, I., Jr., Ritossa, C., & García-Berro, E. 1997, ApJ, 489, 772

Ivezic, Z., Tyson, J. A., Abel, B., et al. 2008, arXiv:0805.2366

Kalirai, J. S. 2012, Nature, 486, 90

Kanaan, A., Kepler, S. O., Giovannini, O., & Diaz, M. 1992, ApJ, 390, L89

Kanaan, A., Nitta, A., Winget, D. E., et al. 2005, A&A, 432, 219

Kennedy, G. M., & Kenyon, S. J. 2008, ApJ, 673, 502

Kepler, S. O., Pelisoli, I., Koester, D., et al. 2016, VizieR Online Data Catalog, 745,

Kilic, M., Munn, J. A., Harris, H. C., et al. 2017, ApJ, 837, 162

Kilic, M., Bergeron, P., Dame, K., et al. 2019, MNRAS, 482, 965

Kleinman, S. J., Kepler, S. O., Koester, D., et al. 2013, ApJS, 204, 5

Koester, D., Gänsicke, B. T., & Farihi, J. 2014, A&A, 566, A34

Korol, V., Rossi, E. M., & Barausse, E. 2019, MNRAS, 483, 5518

Kowalski, P. M., & Saumon, D. 2006, ApJ, 651, L137

Lenz, P., & Breger, M. 2014, Astrophysics Source Code Library, ascl:1407.009

Macfarlane, S. A., Toma, R., Ramsay, G., et al. 2015, MNRAS, 454, 507

Macfarlane, S. A., Woudt, P. A., Groot, P. J., et al. 2017, MNRAS, 465, 434

Manser, C. J., Gänsicke, B. T., Eggl, S., et al. 2019, Science, 364, 66

Massey, P., Strobel, K., Barnes, J. V., & Anderson, E. 1988, ApJ, 328, 315

Miknaitis, G., Pignata, G., Rest, A., et al. 2007, ApJ, 666, 674

Munn, J. A., Harris, H. C., von Hippel, T., et al. 2017, AJ, 153, 10

Pelisoli, I., Kepler, S. O., & Koester, D. 2018, MNRAS,

Parsons, S. G., Gänsicke, B. T., Marsh, T. R., et al. 2013, MNRAS, 429, 256

Parsons, S. G., Gänsicke, B. T., Marsh, T. R., et al. 2017, MNRAS, 470, 4473

Petigura, E. A., Howard, A. W., & Marcy, G. W. 2013, Proceedings of the National Academy of Science, 110, 19273

Pickles, A. J. 1998, PASP, 110, 863

Pollacco, D. L., Skillen, I., Collier Cameron, A., et al. 2006, PASP, 118, 1407

Rappaport, S., Gary, B. L., Kaye, T., et al. 2016, MNRAS, 458, 3904

Rau, A., Kulkarni, S. R., Law, N. M., et al. 2009, PASP, 121, 1334

Rest, A., Stubbs, C., Becker, A. C., et al. 2005, ApJ, 634, 1103

Rest, A., Scolnic, D., Foley, R. J., et al. 2014, ApJ, 795, 44

Robin, A. C., Reylé, C., Derrière, S., & Picaud, S. 2003, A&A, 409, 523

Roelofs, G. H. A., Nelemans, G., & Groot, P. J. 2007, MNRAS, 382, 685

Rowan, D. M., Tucker, M. A., Shappee, B. J., & Hermes, J. J. 2019, MNRAS, 486, 4574

Schechter, P. L., Mateo, M., & Saha, A. 1993, PASP, 105, 1342

Toma, R., Ramsay, G., Macfarlane, S., et al. 2016, MNRAS, 463, 1099

Tonry, J. L., Stubbs, C. W., Kilic, M., et al. 2012, ApJ, 745, 42

Tremblay, P.-E., Bergeron, P., & Gianninas, A. 2011, ApJ, 730, 128

Uytterhoeven, K., Moya, A., Grigahcène, A., et al. 2011, A&A, 534, A125

Vanderburg, A., Johnson, J. A., Rappaport, S., et al. 2015, Nature, 526, 546

Van Sluijs, L., & Van Eylen, V. 2018, MNRAS, 474, 4603

Veras, D., Shannon, A., & Gänsicke, B. T. 2014, MNRAS, 445, 4175

Veras, D. 2016, Royal Society Open Science, 3, 150571

Veras, D., Efroimsky, M., Makarov, V. V., et al. 2019, MNRAS, 486, 3831

Villaver, E., & Livio, M. 2007, ApJ, 661, 1192

Wilson, T. G., Farihi, J., Gänsicke, B. T., & Swan, A. 2019, MNRAS, 487, 133

Winget, D. E., & Kepler, S. O. 2008, ARA&A, 46, 157